MITOCHONDRIAL MORPHOLOGY GOVERNS ATP PRODUCTION RATE

GUADALUPE C. GARCIA[1], KAVYA GUPTA[2], THOMAS M. BARTOL[1], TERRENCE J. SEJNOWSKI[1], AND PADMINI RANGAMANI[2,*]

ABSTRACT. Life is based on energy conversion. In particular, in the nervous system significant amounts of energy are needed to maintain synaptic transmission and homeostasis. To a large extent, neurons depend on oxidative phosphorylation in mitochondria to meet their high energy demand (Pekkurnaz and Wang, 2022). For a comprehensive understanding of the metabolic demands in neuronal signaling, accurate models of ATP production in mitochondria are required. Here, we present a thermodynamically consistent model of ATP production in mitochondria based on previous work (Pietrobon and Caplan, 1985; Magnus and Keizer, 1997; Metelkin et al., 2006; Garcia et al., 2019). The significant improvement of the model is that the reaction rate constants are set such that detailed balance is satisfied. Moreover, using thermodynamic considerations, the dependence of the reaction rate constants on membrane potential, pH, and substrate concentrations are explicitly provided. These constraints assure the model is physically plausible. Furthermore, we explore different parameter regimes to understand in which conditions ATP production or its export are the limiting steps in making ATP available in the cytosol. The outcomes reveal that, under the conditions used in our simulations, ATP production is the limiting step and not its export. Finally, we performed spatial simulations with nine 3D realistic mitochondrial reconstructions and linked the ATP production rate in the cytosol with morphological features of the organelles.

Date: June 29, 2023.

[1] Computational Neurobiology Laboratory, Salk Institute for Biological Studies, La Jolla CA, 92037.

[2] Department of Mechanical and Aerospace Engineering, University of California, San Diego, La Jolla CA 92093.

[*]To whom correspondence should be addressed: e-mail: prangamani@ucsd.edu.

CONTENTS

Abbreviations 3

1. Summary 3

2. Introduction 3

3. Material and Methods 5

3.1. Model for ATP synthase 5

3.2. Model for ATP/ADP translocator (ANT) 11

3.3. Molecular VDAC Model 17

3.4. Metabolite buffers 17

3.5. Simulation methods 18

4. Results 19

4.1. Steady-state flux analysis for the model components and comparison to previously developed models 19

4.2. Under physiological conditions, ATP production is the limiting step for cytosolic ATP availability. 20

4.3. Spatial Simulations: application of the model to different 3D mitochondrial reconstructions 22

5. Discussion 27

6. Data Availability 30

7. Acknowledgments 30

References 30

ABBREVIATIONS

ATP	adenosine triphosphate
ADP	adenosine diphosphate
OM	outer membrane
IM	inner membrane
ETC	electron-transport chain
Pi	inorganic phosphate
CM	cristae membrane
IMS	intermembrane space
VDAC	voltage dependent anion channel
ANT	adenine nucleotide translocator
ODEs	ordinary differential equations

1. SUMMARY

In this work, Garcia et al present a thermodynamically consistent model for ATP production in mitochondria, in which reaction rate constants are set such that detailed balance is satisfied. Simulations revealed that ATP production, but not its export, is the limiting step, and simulations with 3D mitochondrial reconstructions linked the ATP production rate in the cytosol with the morphological features of the organelles.

2. INTRODUCTION

Energy conversion is at the core of cellular function. Finding efficient strategies to transduce energy has driven the evolution of cells and organisms. In eukaryotic cells, respiration occurs in specialized organelles, known as mitochondria. There, metabolic substrates are converted to adenosine triphosphate (ATP), the energy currency of cell (Alberts et al., 2015). Mitochondrial architecture provides an efficient framework for cellular respiration. It is composed of two distinct membranes: the outer membrane (OM) and the inner membrane (IM). The IM is used to generate an electrochemical proton gradient through a series of electron carriers known as the electron-transport chain (ETC) (Figure 1). The energy stored in this gradient drives the synthesis of ATP from adenosine diphosphate (ADP) and inorganic phosphate (Pi), through a multiprotein complex, ATP synthase (Yoshida et al., 2001). The outer membrane plays a central role in controlling the flow of molecules from and to the interior of mitochondria. Although it forms a barrier to large molecules, it contains a large number of proteins, voltage dependent anion channel (VDAC) (Colombini, 2004), that allow the passage of small metabolites and ions. In contrast, the IM is impermeable to molecules; carrier proteins and ion channels are required for molecules to cross this barrier. One of the most relevant carriers is the adenine nucleotide translocator (ANT), which transports ATP and ADP to and from the matrix, the internal region encapsulated by the IM (Figure 1). Overall, this is a membrane-based process that relies on the lipid bilayer of mitochondria to generate the energy required for ATP synthesis.

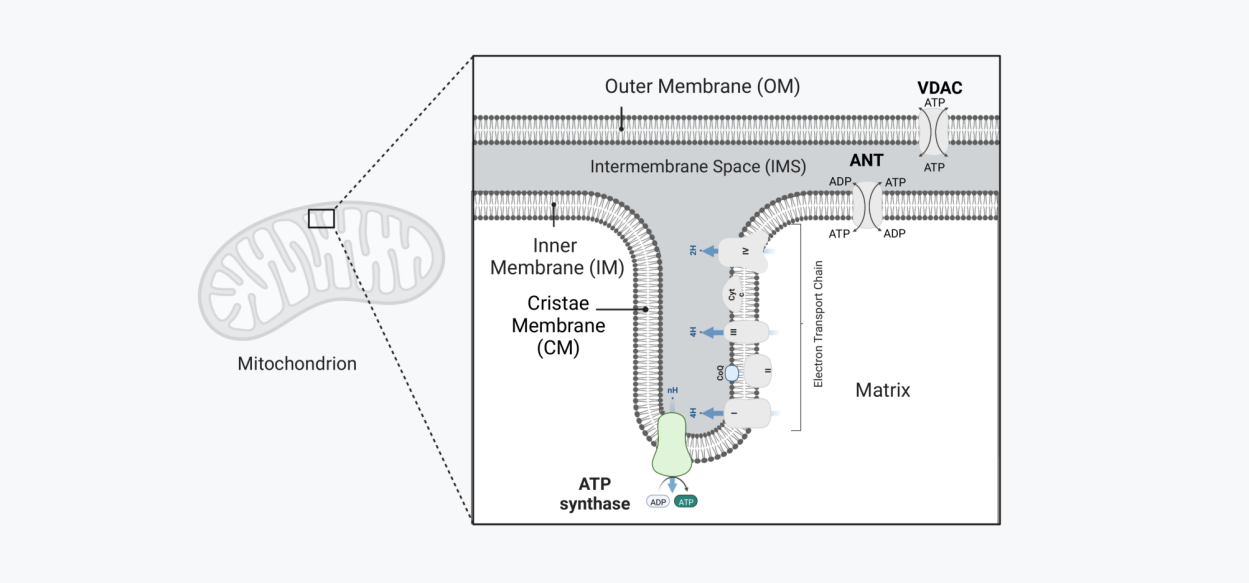

FIGURE 1. Schematic representation of a mitochondrion with its functional components and compartments. The outer membrane (OM) is the external lipid bilayer that interfaces to the cytosol. The inner membrane (IM) encapsulates the matrix, it is composed of two functionally distinct regions, the inner boundary membrane (IBM) (in close opposition to the OM) and the cristae membrane (CM). The cristae membrane (CM) is the place where the protein complexes from the electron-transport chain (ETC) reside. At the apex of the CM and along the tubular cristae ATP synthases are allocated. Through these protein complexes, ATP is synthesized in the matrix. ATP is further transported from the matrix through adenine nucleotide translocators (ANTs) to the intermembrane space (IMS)—the space between the two membranes— to finally cross the OM at the voltage dependent anion channel (VDAC) into the cytosol.

The importance of ATP production by mitochondria means that reliable mathematical formulations are necessary to build a quantitative framework. To that effect, there have been many mathematical models developed to describe the processes involved in ATP production (Pietrobon and Caplan, 1985; Magnus and Keizer, 1997; Cortassa et al., 2003; Nguyen et al., 2007; Bertram et al., 2006; Beard, 2005; Heiske et al., 2017; Garcia et al., 2019). Pietrobon and Caplan 1985 developed a proton pump model, that can be interpreted as a respiration-driven proton pump or as a model of ATP synthase (Magnus and Keizer, 1997). Later on, Magnus and Keizer 1997 assembled different components and built a steady-state model of ATP production in mitochondria, which several other models are based on (Cortassa et al., 2003; Bertram et al., 2006; Nguyen et al., 2007). However, they did not explicitly show how the thermodynamic constraints were imposed to the system[1]. Some of these models also have been built to be consistent with thermodynamic laws (Beard,

[1]These calculations were reported to be in a Ph.D. thesis we could not get access (Magnus, 1995). Recently, we found part of these calculations were included in another PhD thesis (Balbir, 2007)

2005; Heiske et al., 2017), and in most cases include more components as the activity of TCA cycle (Cortassa et al., 2003; Nguyen et al., 2007) enzymes or the activity of other components of the ETC (Beard, 2005; Heiske et al., 2017). Almost all previous developed models are implemented with ordinary differential equations (ODEs), disregarding the spatial organization of mitochondria. Here and in our previous work (Garcia et al., 2019) our efforts were focused on developing a minimal reaction-based mitochondrion model so that we can implement it to perform spatial simulations in MCell (Stiles et al., 1996; Kerr et al., 2008; Husar et al., 2022) or non-spatial simulations. In this work, we ensure the model is thermodynamically consistent, for that we imposed detailed balance constraints to the reaction rate constants.

With the model developed here, we answered the following questions: under physiological conditions, what limits the amount of ATP that reaches the cytosol? Is it the rate of ATP production or is it the rate of ATP export from the mitochondria to the cytosol? To answer these questions, we developed a thermodynamically consistent model of ATP production in mitochondria – i.e. a physically plausible model. Our criteria for thermodynamic consistency was to calculate thermodynamic forces (Hill, 1989) for each cycle in the model and to equate them to the ratio of the forward-to-backward reaction rate constants. In this manner, we verified that detailed balance is satisfied for the conditions considered. Furthermore, we calculated the dependence of the reaction rate constants on the membrane potential, pH, ATP, ADP, and Pi concentrations. We conducted simulations of this model using ODEs; although simpler, this approach is informed with detailed structural calculations of surface areas and volumes from a realistic 3D reconstruction (Garcia et al., 2019). The outcomes reveal that, under physiological conditions, ATP production in the matrix is the limiting factor. Lastly, we used the model to perform spatial simulations using nine realistic 3D reconstructions (Mendelsohn et al., 2021). Our results link the ATP production rate to structural features of the mitochondrial geometries.

3. Material and Methods

The model presented here is based on previous work (Pietrobon and Caplan, 1985; Magnus and Keizer, 1997; Metelkin et al., 2006; Garcia et al., 2019). Our efforts were focused on assembling a thermodynamically consistent model (Hill, 1989), and explicitly highlighting the dependence of the reaction rates constants on the membrane potential, pH, ATP, ADP, and Pi concentration.

3.1. **Model for ATP synthase.** The ATP synthase model is grounded on the work of Pietrobon and Caplan 1985. The kinetic model consists of a membrane protein –represented as E– that transports protons (H^+) from the intermembrane space (IMS) to the matrix. The protein can be in six states represented in Figure 2A. Each state has associated a number from 1 to 6 (Figure 2B). A clockwise cycle starting in state 6 (E^{-3}) represents the binding of 3 protons from the IMS (transition 6 $\rightarrow$ 5 in Figure 2B), transport of the protons to the matrix (state 5 $\rightarrow$ 4), binding of ADP and P_i (state 4 $\rightarrow$ 3) and subsequent synthesis of ATP (state 3 $\rightarrow$ 2), followed by unbinding of the protons in the matrix (state 2 $\rightarrow$ 1). We considered a constant proton concentration inside the IMS and the matrix, and the ATP and ADP concentration as variables. The list of the reactions is given in Table 1 and the model parameters are given in Table 2. The number of ATP synthases used in the

model was determined employing the density estimated at 3070 μm^{-2} (Acehan et al., 2011). Given the surface area of high curvature of the IM in the reconstructions (Mendelsohn et al., 2021), we estimated the number of ATP synthases at 267 for the mitochondrial reconstruction #1 (Mito 1). We next explain how some kinetic parameters depend on the membrane potential, the proton concentration, and the phosphate concentration.

List of Reactions for the ATP synthase model
$^{-3}\mathrm{E} + 3\mathrm{H}^+_\mathrm{m} \underset{k_{21}}{\overset{k_{12}}{\rightleftharpoons}} \mathrm{H_3E}$
$\mathrm{H_3E} + \mathrm{T}^+_\mathrm{m} \underset{k_{32}}{\overset{k_{23}}{\rightleftharpoons}} \mathrm{H_3ES}$
$\mathrm{H_3ES} \underset{k_{43}}{\overset{k_{34}}{\rightleftharpoons}} \mathrm{H_3E^*} + \mathrm{D_m}$
$\mathrm{H_3E^*} \underset{k_{54}}{\overset{k_{45}}{\rightleftharpoons}} \mathrm{EH_3}$
$\mathrm{EH_3} \underset{k_{65}}{\overset{k_{56}}{\rightleftharpoons}} \mathrm{E}^{-3} + \mathrm{H}^+_\mathrm{i}$
$\mathrm{E}^{-3} \underset{k_{16}}{\overset{k_{61}}{\rightleftharpoons}} {}^{-3}E$

TABLE 1. List of reactions for the ATP synthase model.

3.1.1. *Thermodynamic constraints.* Thermodynamic constraints are imposed on the rate constants of the system. At an arbitrary steady-state, the product of the first-order (or pseudo-first order) rate constants around a cycle κ in the positive direction ($\prod_{\kappa^+}$) divided by the product of the rate constants in the negative direction ($\prod_{\kappa^-}$) is related to net thermodynamic forces in the following manner (Hill, 1989):

$$\frac{\prod_{\kappa^+}}{\prod_{\kappa^-}} = \mathrm{e}^{(\frac{\chi}{\mathrm{RT}})} = \mathrm{e}^{(\frac{\Delta \mathrm{G}_\kappa}{\mathrm{RT}})}, \tag{3.1}$$

where χ is the net thermodynamic force, $\Delta \mathrm{G}_\kappa$ is the difference in Gibbs free energy per mole of substance (i.e. the chemical potential) in the cycle κ, R is the universal gas constant and T is the absolute temperature. At thermodynamic equilibrium, and in absence of a potential difference between the membranes, the ΔG in the cycle is zero. This leads to a ratio of forward rate constants to backward rate constants equal to one (Eqs 3.1), also known as detailed balance.

Starting with the shortest cycle, **b** in the diagram (Figure 2C) we obtain:

$$\frac{\prod_{\mathrm{b}^+}}{\prod_{\mathrm{b}^-}} = \mathrm{e}^{(\frac{\chi}{\mathrm{RT}})} = \mathrm{e}^{(\frac{\Delta \mathrm{G_b}}{\mathrm{RT}})}. \tag{3.2}$$

Replacing the rate constants in the cycle we get:

$$\frac{\mathrm{k_{12}k_{25}k_{56}k_{61}}}{\mathrm{k_{21}k_{52}k_{65}k_{16}}} = \mathrm{K_{12}K_{25}K_{56}K_{61}}, \tag{3.3}$$

where $\mathrm{K_{ij}}$ are the equilibrium constants of the transitions from state i to state j. The equilibrium constants are given by (Caplan and Essig, 1983):

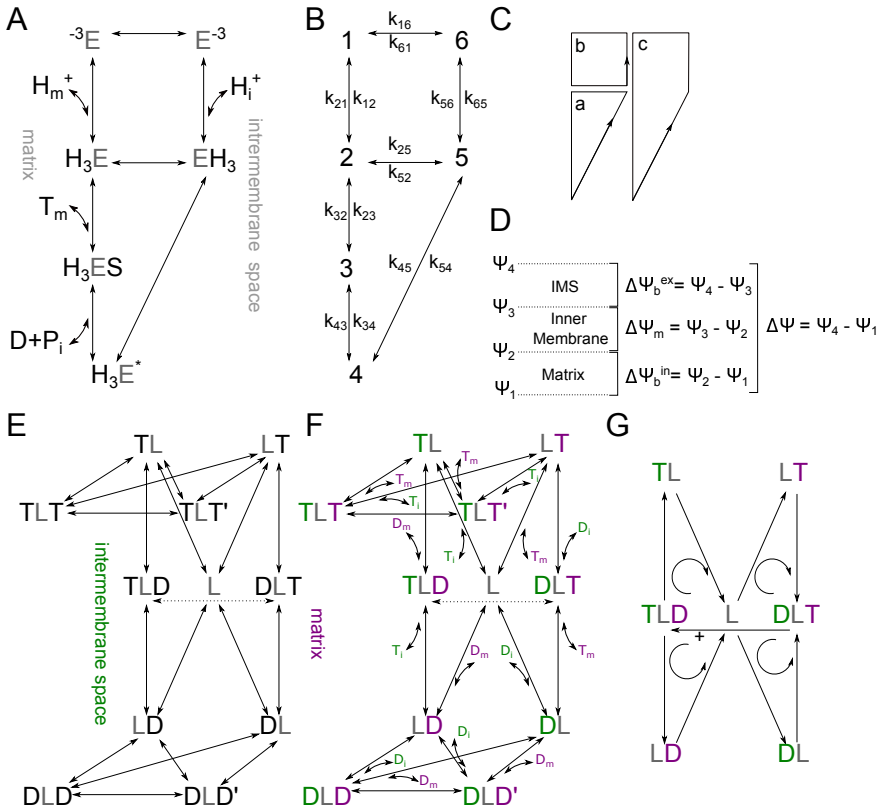

FIGURE 2. Kinetic diagram of the modules of the mitochondria model. (A-C) Kinetic diagram of the ATP synthase model (Pietrobon and Caplan, 1985). (A) The model consists of six states, representing different protein configurations. ATP molecules are represented as T, ADP molecules as D, Phosphate as $\mathrm{P_i}$, ATP synthase as E, and H^+ as protons. The model considers the binding of ATP and ADP from the matrix and the IMS. (B) Each state has associated a number from 1 to 6. A clockwise cycle, starting from state 6 corresponds to the binding of 3 protons from the IMS ($6 \rightarrow 5$), followed by their transport to the matrix ($5 \rightarrow 4$) and subsequent binding of ADP and $\mathrm{P_i}$ ($4 \rightarrow 3$), to the synthesis of ATP ($3 \rightarrow 2$), and unbinding of 3 protons in the matrix ($2 \rightarrow 1$). Each transition has an associated rate constant $\mathrm{k_{ij}}$. The list of all the reactions is in Table 1 and the list of parameters is in Table 2. (C) The cycles are considered positive in the counter-clockwise direction and named a, b, and c. (D) Membrane potential considered in the ATP synthase model. $\Delta\Psi = \Psi_4 - \Psi_1$ is the electrical potential difference between the matrix and IMS (or cytosol), $\Delta\Psi_m$ is the electrical potential difference across the membrane, $\Delta\Psi_{\mathrm{b}}^{\mathrm{in}}$ and $\Delta\Psi_{\mathrm{b}}^{\mathrm{ex}}$ are the phase-boundary potentials. (E)-(G) Kinetic diagram of the ANT model. (E) The model consists of 11 states, L represents the free protein, and YLX is a triple molecular state with one X molecule bound from the matrix side and one Y molecule bound from the IMS. X and Y represent ATP or ADP molecules respectively. The model has been adapted from previous work (Metelkin et al., 2006). (F) In this representation, the binding and unbinding of ATP and ADP are explicitly shown, molecules from the IMS side are in green, and those from the matrix side are in purple. (G) The cycles are considered positive going from the matrix to the IMS.

$$K_{ij} = \frac{k_{ij}}{k_{ji}} = e^{\frac{G_i - G_j}{RT}}, \tag{3.4}$$

where G_i and G_j are the Gibbs free energy per mole for species in states i and j respectively. The equilibrium constant for the transition from state 1 to 2, where three protons bind from the matrix side, is equal to:

$$K_{12} = \frac{k_{12}}{k_{21}} = e^{\frac{G_1 - G_2}{RT}}, \tag{3.5}$$

where G_1 is the Gibbs free energy per mole of three protons in the matrix and G_2 the energy of the protons bound to the membrane. These are given by (Caplan and Essig, 1983):

$$G_1 = G_1^o + 3F\Psi_1 + 3RT\ln([H_m^+]),\ G_2 = G_2^o + 3F\Psi_2, \tag{3.6}$$

where G_1^o and G_2^o are the standard free energy per mole. Here Ψ_1 is the bulk potential at the matrix, Ψ_2 is the phase boundary potential at the surface of the inner membrane (Figure 2D), and F is the Faraday's constant. Replacing Eq. 3.6 in Eq. 3.5 we arrive at:

$$\frac{k_{12}}{k_{21}} = e^{(\frac{G_1^o - G_2^o}{RT})} e^{(\frac{-3F\Delta\Psi_b^{in}}{RT})} [H_m^+]^3, \tag{3.7}$$

where $\Delta\Psi_b^{in} = \Psi_2 - \Psi_1$ is the phase-boundary potential (the difference between the bulk potential and the potential at the surface of the membrane, see Figure 2D), and $[H_m^+]$ is the proton concentration in the matrix. We define $k_{ij,0}$ as the rate constants at zero potential difference and k_{ij}^* as the rate constants independent of the concentrations; we arrive at:

$$\frac{k_{12}}{k_{21}} = \frac{k_{12}^*}{k_{21,0}} e^{(\frac{-3F\Delta\Psi_b^{in}}{RT})} [H_m^+]^3. \tag{3.8}$$

Following the original model (Pietrobon and Caplan, 1985), we assign the effect of the phase-boundary potentials to the unbinding rate constant k_{21}, and proton concentration to the binding rate constant k_{12}:

$$k_{21} = k_{21,0} e^{(\frac{3F\Delta\Psi_b^{in}}{RT})},\ k_{12} = k_{12}^* [H_m^+]^3. \tag{3.9}$$

We take a similar approach for the transition $6 \rightarrow 5$, where three protons bind from the IMS to the inner membrane. The Gibbs energy per mole for the protons in the IMS (G_6) and bound to the membrane (G_5) are:

$$G_6 = G_6^o + 3F\Psi_4 + 3RT\ln([H_i^+]),\ G_5 = G_5^o + 3F\Psi_3. \tag{3.10}$$

Replacing Eq. 3.10 in Eq. 3.4 we arrive at:

$$K_{65} = \frac{k_{65}}{k_{56}} = e^{(\frac{G_6^o - G_5^o}{RT})} e^{(\frac{-3F\Delta\Psi_b^{ex}}{RT})} [H_i^+]^3, \tag{3.11}$$

where $\Delta\Psi_b^{ex} = \Psi_4 - \Psi_3$ is the phase-boundary potential from the IMS, and H_i^+ is the proton concentration in the IMS.

As before, we can rewrite Eq. 3.11 with the rate constant at zero potential difference and the rate constant independent of the concentration as:

$$\frac{k_{65}}{k_{56}} = \frac{k_{65}^*}{k_{56,0}} e^{(\frac{-3F\Delta\Psi_b^{ex}}{RT})} [H_i^+]^3. \tag{3.12}$$

The effect of the phase-boundary potentials is assigned to the unbinding rate constants k_{56}, and the proton concentration to the binding rate constant k_{65} and we obtain:

$$k_{56} = k_{56,0} e^{(\frac{3F\Delta\Psi_b^{ex}}{RT})},\ k_{65} = k_{65}^* [H_i^+]^3. \tag{3.13}$$

The transition from state $1 \rightarrow 6$ involves the movement of the negatively charged proton biding site from the matrix to the IMS. Therefore the Gibbs free energy for this transition can be written as:

$$G_1 = G_1^o - 3F\Psi_2,\ G_6 = G_6^o - 3F\Psi_3. \tag{3.14}$$

Here, Ψ_2 and Ψ_3 are the potentials at the respective membrane surfaces (Figure 2). Replacing in Eq. 3.4 we arrive at:

$$K_{16} = \frac{k_{16}}{k_{61}} = e^{(\frac{G_1^o - G_6^o}{RT})} e^{(\frac{3F\Delta\Psi_m}{RT})}, \tag{3.15}$$

where $\Delta\Psi_m = \Psi_3 - \Psi_2$. As before, replacing with the rate constants at zero membrane potential difference we reach:

$$\frac{k_{16}}{k_{61}} = \frac{k_{16,0}}{k_{61,0}} e^{(\frac{3F\Delta\Psi_m}{RT})}. \tag{3.16}$$

Following the original model (Pietrobon and Caplan, 1985), we considered a symmetrical Eyring barrier (Caplan, 1981). With this assumption the individual rate constants can be written as:

$$k_{16} = k_{16,0} e^{(\frac{3F\Delta\Psi_m}{2RT})},\ k_{61} = k_{61,0} e^{(\frac{-3F\Delta\Psi_m}{2RT})}. \tag{3.17}$$

Substituting the equilibrium rate constants calculated above in Eqs. 3.3 we arrive at:

$$\frac{k_{12}k_{25}k_{56}k_{61}}{k_{21}k_{52}k_{65}k_{16}} = \frac{k_{12}^*}{k_{21,0}} e^{(\frac{-3F\Delta\Psi_b^{in}}{RT})} [H_m^+]^3 \frac{k_{25}}{k_{52}} \frac{k_{56,0}}{k_{65}^*} e^{(\frac{3F\Delta\Psi_b^{ex}}{RT})} [H_i^+]^{-3} \frac{k_{61,0}}{k_{16,0}} e^{(\frac{-3F\Delta\Psi_m}{RT})}. \tag{3.18}$$

At thermodynamic equilibrium, detailed balance impose an additional constraint to the rate constants:

$$\frac{k_{12}^{*}k_{25}k_{56,0}k_{61,0}}{k_{21,0}k_{52}k_{65}^{*}k_{16,0}} = 1, \tag{3.19}$$

which yields:

$$\frac{\prod_{b^{+}}}{\prod_{b^{-}}} = e^{\frac{-3F(\Delta\Psi_{m}-\Delta\Psi_{b}^{ex}+\Delta\Psi_{b}^{in})}{RT}} \frac{[H_{m}^{+}]^{3}}{[H_{i}^{+}]^{3}} = e^{(\frac{-3F\Delta p}{RT})}. \tag{3.20}$$

Here Δp is the proton motive force:

$$\Delta p = \Delta\Psi - 2.303\,\frac{RT}{F}\Delta pH, \tag{3.21}$$

where $\Delta\Psi$ is the total potential difference across the matrix and the IMS, and ΔpH is the pH difference across the IMS and the matrix ($\Delta pH = pH_{i} - pH_{m}$). Similarly for the cycle **a** (Figure 2C) we obtain:

$$\frac{\prod_{a^{+}}}{\prod_{a^{-}}} = \frac{k_{23}k_{34}k_{45}k_{52}}{k_{32}k_{43}k_{54}k_{25}} = e^{\frac{\chi_{a}}{RT}}, \tag{3.22}$$

where χ_{a} is the thermodynamic force given by:

$$\chi_{a} = RT\ \ln(K\frac{[ATP]}{[ADP][Pi]}), \tag{3.23}$$

where K is the equilibrium constant of the ATP hydrolysis reaction. At equilibrium, we arrive at:

$$\frac{k_{23}k_{34}k_{45}k_{52}}{k_{32}k_{43}k_{54}k_{25}} = 1. \tag{3.24}$$

This yields:

$$\frac{k_{23}^{*}k_{34}k_{45}k_{52}}{k_{32}k_{43}^{*}k_{54}k_{25}} = K, \tag{3.25}$$

imposing further constraints on the rate constants. Finally, for the longest cycle **c**, the thermodynamic force is the sum of forces for cycles **b** and **a**:

$$\Delta G_{c} = \chi_{a} - 3F\Delta p = RT\ \ln(K\frac{[ATP]}{[ADP][Pi]}) - 3F(\Delta\Psi - 2.303\,\frac{RT}{F}\Delta pH). \tag{3.26}$$

As before the product of the reaction rate constants relates to the thermodynamic forces in the following manner:

$$\frac{\prod_{c^+}}{\prod_{c^-}} = \frac{k_{23}k_{34}k_{45}k_{52}}{k_{32}k_{43}k_{54}k_{25}} = e^{\frac{\chi_a}{RT}} e^{\frac{-3F\Delta p}{RT}}, \tag{3.27}$$

which at equilibrium can be expressed as:

$$\frac{k^*_{23}k_{34}k_{45}k_{52}}{k_{32}k^*_{43}k_{54}k_{25}} = Ke^{\frac{-3F\Delta p}{RT}}, \tag{3.28}$$

imposing further constraints on the rate constants.

We use the chemical reactions and rate constants presented above to implement the system using compartmental ODEs. As a result of our calculations, the system of ODEs for the ATP synthase model is given by:

$$\begin{aligned}
\frac{dE^{-3}}{dt} &= -k_{65}\,E^{-3} + k_{56}\,EH_3 + k_{16}\,{}^{-3}E - k_{61}\,E^{-3},\\
\frac{d\,{}^{-3}E}{dt} &= -k_{16}\,{}^{-3}E + k_{61}\,E^{-3} - k_{12}\,{}^{-3}E + k_{21}\,H_3E,\\
\frac{dH_3E^*}{dt} &= -k_{45}\,H_3E^* + k_{54}\,EH_3 + k_{34}\,H_3ES - k_{43}\,H_3E^*\,D_m,\\
\frac{dH_3ES}{dt} &= k_{43}\,D_m\,H_3E^* - k_{34}\,H_3ES + k_{23}\,H_3E\,T_m - k_{32}\,H_3ES,\\
\frac{dH_3E}{dt} &= -k_{23}\,H_3E\,T_m + k_{32}\,H_3ES - k_{25}\,H_3E + k_{52}\,EH_3 + k_{12}\,{}^{-3}E - k_{21}\,H_3E.
\end{aligned} \tag{3.29}$$

where variables E^{-3},${}^{-3}E$, etc, are the number of molecules in the different states. The rate constants of the bimolecular reactions have been normalized to have proper units to compute the number of particles, i.e. $k = \frac{k'}{N_A V}$, where k' represents the constants given in Table 2, N_A is the Avogadro's number, and V represents the volume. The volume is either the volume of the matrix or the IMS depending on where the specific reaction occurs (see section 3.5 Simulations Methods). These five differential equations describe the dynamic of the ATP synthase model. The dynamic of the missing state EH_3 can be deduced, since the total number of proteins is a conserved quantity (E_{tot}), leading to the conservation expression $E^{-3} + EH_3 + H_3E + H_3ES + H_3E^* + {}^{-3}E = E_{tot}$. E_{tot} is the total number of ATP synthases considered in the simulations, this parameter is $\#ATP_{syn1}$ in Table 2.

3.2. **Model for ATP/ADP translocator (ANT).** The ANT model is based on the work of (Metelkin et al., 2006). It is composed of 11 states and 20 bidirectional transitions. The kinetic diagram is shown in Figure 2F. The free protein (L) can bind molecules from the matrix (on the right) or IMS side (on the left), forming a triple molecular state (YLX), where Y and X represent ATP or ADP. State YLX can transition to state XLY exporting X to the IMS and importing Y, following unbinding of the molecules. The productive transition that exports ATP is DLT $\rightarrow$ TLD, and the reversal reaction imports ATP to the matrix and exports ADP to the IMS. Two additional states (DLD'

Parameter	Definition	Value	Unit	Reference
F	Faraday's constant	9.649×10^{4}	$C\,mol^{-1}$	(Keener and Sneyd, 1998)
R	Universal gas constant	8.315	$J\,mol^{-1}\,K^{-1}$	(Keener and Sneyd, 1998)
pH_m	Matrix pH	7.6		(Magnus and Keizer, 1997
pH_c	Cristae pH	7.2		(Magnus and Keizer, 1997
[Pi]	Phosphate concentration	20	mM	(Pietrobon and Caplan, 198
T	Temperature	310	K	
K	Equilibrium constant	1.71×10^{6}	M	(Pietrobon and Caplan, 198
$\Delta\psi$	Membrane potential	180	mV	(Holmuhamedov et al., 199
$\Delta\psi_{B,i}$	Phase boundary potential	−50	mV	(Pietrobon and Caplan, 198
$\Delta\psi_{B,M}$	Phase boundary potential	0	mV	(Pietrobon and Caplan, 198
$k_{61,0}$	Rate constant at 0 mV	4.98×10^{7}	s^{-1}	(Pietrobon and Caplan, 198
$k_{16,0}$	Rate constant at 0 mV	1×10^{2}	s^{-1}	(Pietrobon and Caplan, 198
$k_{56,0}$	Rate constant at 0 mV	2.75×10^{5}	s^{-1}	(Pietrobon and Caplan, 198
$k_{21,0}$	Rate constant at 0 mV	40	s^{-1}	(Pietrobon and Caplan, 198
k^*_{43}	Rate constant†	1×10^{8}	$M^{-2}\,s^{-1}$	(Pietrobon and Caplan, 198
k^*_{12}	Rate constant †	6.33×10^{24}	$M^{-3}\,s^{-1}$	(Pietrobon and Caplan, 198
k^*_{65}	Rate constant†	1.58×10^{25}	$M^{-3}\,s^{-1}$	(Pietrobon and Caplan, 198
k^*_{23}	Rate constant†	5×10^{6}	$M^{-1}\,s^{-1}$	(Pietrobon and Caplan, 198
k_{54}	Rate constant	1×10^{2}	s^{-1}	(Pietrobon and Caplan, 198
k_{32}	Rate constant	5×10^{3}	s^{-1}	(Pietrobon and Caplan, 198
k_{34}	Rate constant	100	s^{-1}	(Pietrobon and Caplan, 198
k_{45}	Rate constant	100	s^{-1}	(Pietrobon and Caplan, 198
k_{56}	Rate constant	1000	s^{-1}	(Pietrobon and Caplan, 198
k_{25}	Rate constant	5.85×10^{-30}	s^{-1}	(Pietrobon and Caplan, 198
k_{52}	Rate constant	1×10^{-20}	s^{-1}	(Pietrobon and Caplan, 198
k_{43}	Rate constant‡	2×10^{6}	$M^{-1}\,s^{-1}$	(Pietrobon and Caplan, 198
k_{12}	Rate constant‡	25	s^{-1}	(Pietrobon and Caplan, 198
k_{65}	Rate constant‡	3969	s^{-1}	(Pietrobon and Caplan, 198
k_{61}	Rate constant at 180 mV	33 989	s^{-1}	(Pietrobon and Caplan, 198
k_{16}	Rate constant at 180 mV	146 516	s^{-1}	(Pietrobon and Caplan, 198
k_{56}	Rate constant at 180 mV	1000	s^{-1}	(Pietrobon and Caplan, 198
k_{21}	Rate constant at 180 mV	40	s^{-1}	(Pietrobon and Caplan, 198
δ_{atp}	Density of ATP synthases	3070	μm^{-2}	(Acehan et al., 2011)
$\#ATP_{syn1}$	Number of ATP synthases for Mito #1	267		*

TABLE 2. Parameters for the ATP synthase model. * Our estimation, given the surface area of high curvature of the IM measured in the reconstruction (Mendelsohn et al., 2021). †independent of the concentration. ‡ concentration dependent.

and TLT') were added to track futile translocation (exchange of ADP for ADP and ATP for ATP). Starting from previously fitted flux parameters (Metelkin et al., 2006) for ANTs extracted from heart mitochondria (Kraemer and Klingenberg, 1982), we first estimated the parameters of the dynamic implementation of the model. With this set of parameters, we qualitatively reproduced the independent data from published work (Kraemer and Klingenberg, 1982; Duyckaerts et al., 1980). The rate constants of the model are presented in Tables 4 and 5, and the qualitative reproduction of the experimental data is in Supplementary Figure 1 and Supplementary Figure 2.

List of Reactions for the ANT model
$T_m + L \underset{k^-_{T_m}}{\overset{k^+_{T_m}}{\longleftrightarrow}} LT$
$D_m + L \underset{k^-_{D_m}}{\overset{k^+_{D_m}}{\longleftrightarrow}} LD$
$T_i + L \underset{k^-_{T_i}}{\overset{k^+_{T_i}}{\longleftrightarrow}} TL$
$D_i + L \underset{k^-_{D_i}}{\overset{k^+_{D_i}}{\longleftrightarrow}} DL$
$T_i + LT \underset{k^-_{T_i}}{\overset{k^+_{T_i}}{\longleftrightarrow}} TLT$
$D_i + LT \underset{k^-_{D_i}}{\overset{k^+_{D_i}}{\longleftrightarrow}} DLT$
$T_i + LD \underset{k^-_{D_i}}{\overset{k^+_{D_i}}{\longleftrightarrow}} TLD$
$D_i + LD \underset{k^-_{D_i}}{\overset{k^+_{D_i}}{\longleftrightarrow}} DLD$
$TLD \xrightarrow{k_{cp}} DLT$
$DLT \xrightarrow{k_p} TLD$
$TLT \xrightarrow{k_t} TLT'$
$TLT' \xrightarrow{k_t} TLT$
$DLD \xrightarrow{k_d} DLD'$
$DLD' \xrightarrow{k_d} DLD$

TABLE 3. List of Reactions for the ANT model.

3.2.1. *Thermodynamic constrains.* As presented in the previous section the parameters of the ANT model are constrained by thermodynamic considerations (Eq. 3.1). If we consider a positive cycle a productive translocation of one ATP from the matrix to the IMS and ADP from the IMS to the matrix (Figure 2G), the product of the rate constants in the positive cycle ($\prod_{\kappa^+}$) divided by the product of the rate constants in the negative cycle ($\prod_{\kappa^-}$) can be written as:

$$\frac{\prod_{\kappa^+}}{\prod_{\kappa^-}} = \frac{k^+_{T_m}[T_m]k^+_{D_i}[D_i]k_p k^-_{T_i} k_{D_m}}{k^+_{D_m}[D_m]k^+_{T_i}[T_i]k_{cp} k^-_{D_i} k^-_{T_m}}. \tag{3.30}$$

Parameter	Value	Unit
$k^{-}_{T_m}$	4×10^{4}	s^{-1}
$k^{+}_{T_m}$	6.4×10^{6}	$M^{-1}\,s^{-1}$
$k^{-}_{T_i}$	200	s^{-1}
$k^{+}_{T_i}$	4×10^{5}	$M^{-1}\,s^{-1}$
$k^{-}_{D_m}$	4×10^{4}	s^{-1}
$k^{+}_{D_m}$	4×10^{6}	$M^{-1}\,s^{-1}$
$k^{-}_{D_i}$	100	s^{-1}
$k^{+}_{D_i}$	4×10^{6}	$M^{-1}\,s^{-1}$
k_p	9.2	s^{-1}
k_{cp}	0.35	s^{-1}
k_d	0.48	s^{-1}
k_t	0.58	s^{-1}
T	310	K
$\Delta\psi$	180	mV
δ_{ANTs}	1.37	nmol/mg prot*
$\#ANTs_1$	16471 **	

TABLE 4. Parameters for the ANT model at $\Delta\psi = 180\,\mathrm{mV}$.
* We estimated 1 nmol/mg $\approx$ 1.25 mM. ** We used the volume of the IM to get the final number of ANTs.

Parameter	Value	Unit
$k^{-}_{T_m}$	4.4×10^{4}	s^{-1}
$k^{+}_{T_m}$	6.4×10^{6}	$M^{-1}\,s^{-1}$
$k^{-}_{T_i}$	200	s^{-1}
$k^{+}_{T_i}$	4.8×10^{6}	$M^{-1}\,s^{-1}$
$k^{-}_{D_m}$	4×10^{4}	s^{-1}
$k^{+}_{D_m}$	4×10^{6}	$M^{-1}\,s^{-1}$
$k^{-}_{D_i}$	100	s^{-1}
$k^{+}_{D_i}$	4×10^{6}	$M^{-1}\,s^{-1}$
k_p	0.15	s^{-1}
k_{cp}	0.35	s^{-1}
k_d	0.48	s^{-1}
k_t	0.78	s^{-1}
T	310	K
$\Delta\psi$	0	mV

TABLE 5. Parameters for the ANT model at $\Delta\psi = 0\,\mathrm{mV}$.

Here k^- are the backward rate constants and k^+ are the forward rate constants for ATP (T) or ADP (D) from the matrix side (m) or the IMS (i), respectively. Replacing with the dissociation constants (the ratio of the backward to forward reaction rates) we arrive at:

$$\frac{\prod_{\kappa^+}}{\prod_{\kappa^-}} = \frac{\mathrm{K_{T_i} K_{D_m} k_p [T_m][D_i]}}{\mathrm{K_{D_i} K_{T_m} k_{cp} [D_m][T_i]}}, \tag{3.31}$$

where $[\mathrm{D_m}]$,$[\mathrm{T_m}]$,$[\mathrm{T_i}]$ and $[\mathrm{D_i}]$ are the concentrations of ADP and ATP in the matrix and IMS respectively. The Gibbs free energy per mole associated with the species before the translocation are:

$$\begin{aligned} \mathrm{G_i} &= \mathrm{RT}\ln([\mathrm{T_m}]) + \mathrm{z_t F}\psi_1 + \mathrm{RT}\ln([\mathrm{D_i}]) + \mathrm{z_D F}\psi_4, \\ \mathrm{G_o} &= \mathrm{RT}\ln([\mathrm{T_i}]) + \mathrm{z_t F}\psi_4 + \mathrm{RT}\ln([\mathrm{D_m}]) + \mathrm{z_D F}\psi_1, \end{aligned} \tag{3.32}$$

where $\mathrm{z_t}$ and $\mathrm{z_d}$ are the charge of the ionized forms of ATP and ADP, –4 and –3 respectively. So the difference in Gibbs free energy per mole associated with the translocation of an ionized ATP molecule from the matrix to the IMS, against a concentration gradient and the translocation of an ionized ADP molecule from the matrix to the IMS is equal to:

$$\Delta\mathrm{G} = \mathrm{G_i} - \mathrm{G_o} = \mathrm{RT}\ln(\frac{[\mathrm{T_m}][\mathrm{D_i}]}{[\mathrm{T_i}][\mathrm{D_m}]}) + \mathrm{F}(\psi_4 - \psi_1). \tag{3.33}$$

Combining Eq. 3.31 and Eq. 3.33 we arrive at:

$$\frac{\mathrm{K_{T_i} K_{D_m} k_p [T_m][D_i]}}{\mathrm{K_{D_i} K_{T_m} k_{cp} [D_m][T_i]}} = \mathrm{e}^{\ln \frac{[\mathrm{T_m}][\mathrm{D_i}]}{[\mathrm{T_i}][\mathrm{D_m}]}} \mathrm{e}^{\frac{\mathrm{F}\Delta\psi}{\mathrm{RT}}}, \tag{3.34}$$

which reduces to:

$$\frac{\mathrm{K_{T_i} K_{D_m} k_p}}{\mathrm{K_{D_i} K_{T_m} k_{cp}}} = \mathrm{e}^{\frac{\mathrm{F}\Delta\psi}{\mathrm{RT}}}. \tag{3.35}$$

This equation summarizes the imposing restrictions on the rate constants.

The differential equations for the number of molecules of the ANT model in the different states are:

$$
\begin{aligned}
\frac{dL}{dt} &= -(k^{+}_{T_i}\,T_i + k^{+}_{T_m}\,T_m + k^{+}_{D_i}\,D_i + k^{+}_{D_m}\,D_m)\,L + k^{-}_{T_i}\,TL + k^{-}_{T_m}\,LT + k^{-}_{D_i}\,DL + k^{-}_{D_m}\,LD,\\
\frac{dTL}{dt} &= k^{+}_{T_i}\,T_i\,L - (k^{-}_{T_i} + k^{+}_{D_m}\,D_m + 2k^{+}_{T_m}\,T_m)\,TL + k^{-}_{T_m}\,TLT + k^{-}_{T_m}\,TLT' + k^{-}_{D_m}\,TLD,\\
\frac{dLT}{dt} &= k^{+}_{T_m}\,T_m\,L - (k^{-}_{T_m} + k^{+}_{D_i}\,D_i + 2k^{+}_{T_i}\,T_i)\,LT + k^{-}_{T_i}\,TLT + k^{-}_{T_i}\,TLT' + k^{-}_{D_i}\,DLT,\\
\frac{dDL}{dt} &= k^{+}_{D_i}\,D_i\,L - (k^{-}_{D_i} + k^{+}_{T_m}\,T_m + k^{+}_{D_m}\,D_m)\,DL + k^{-}_{D_m}\,DLD + k^{-}_{D_m}\,DLD' + k^{-}_{T_m}\,DLT,\\
\frac{dLD}{dt} &= k^{+}_{D_m}\,D_m\,L - (k^{-}_{D_m} + k^{+}_{T_i}\,T_i + k^{+}_{D_i}\,D_i)\,LD + k^{-}_{D_i}\,DLD + k^{-}_{D_i}\,DLD' + k^{-}_{T_i}\,TLD,\\
\frac{dTLD}{dt} &= k^{+}_{D_m}\,D_m\,TL + k^{+}_{T_i}\,T_i\,LD - (k^{-}_{D_m} + k_{cp})\,TLD + k_p\,DLT - k^{-}_{T_i}\,TLD,\\
\frac{dDLD}{dt} &= k^{+}_{D_i}\,0.5\,D_i\,LD + k^{+}_{D_m}\,0.5\,D_m\,DL - (k^{-}_{D_i} + k^{-}_{D_m} + k_d)\,DLD + k_d\,DLD',\\
\frac{dDLD'}{dt} &= k^{+}_{D_i}\,0.5\,D_i\,LD + k^{+}_{D_m}\,0.5\,D_m\,DL - (k^{-}_{D_i} + k^{-}_{D_m} + k_d)\,DLD' + k_d\,DLD,\\
\frac{dTLT}{dt} &= k^{+}_{T_i}\,0.5\,T_i\,LT + k^{+}_{T_m}\,0.5\,T_m\,TL - (k^{-}_{T_i} + k^{-}_{T_m} + k_t)\,TLT + k_t\,TLT',\\
\frac{dTLT'}{dt} &= k^{+}_{T_i}\,0.5\,T_i\,LT + k^{+}_{T_m}\,0.5\,T_m\,TL - (k^{-}_{T_i} + k^{-}_{T_m} + k_t)\,TLT' + k_t\,TLT.
\end{aligned}
\tag{3.36}
$$

A vast majority of the models do not consider ATP and ADP concentrations as variables (Magnus and Keizer, 1997; Cortassa et al., 2003). Because we focused on the local cytosolic environment around a single mitochondrion, we consider ATP and ADP concentrations in the different compartments as variables. To account for their dynamics, we also derived the equations for the number of ATP and ADP molecules in the different compartments:

$$
\begin{aligned}
\frac{dD_m}{dt} &= -\,(k^{+}_{D_m}\,L + k^{+}_{D_m}\,TL + k^{+}_{D_m}\,DL + k_{43}\,H_3E_o)\,D_m + k^{-}_{D_m}\,LD + k^{-}_{D_m}\,TLD, \qquad (3.37)\\
&\quad + k^{-}_{D_m}\,DLD + k^{-}_{D_m}\,DLD' + k_{34}\,H_3ES,\\
\frac{dT_m}{dt} &= -\,(k^{+}_{T_m}\,L + k^{+}_{T_m}\,TL + k^{+}_{T_m}\,DL + k_{23}\,H_3E)\,T_m + k^{-}_{T_m}\,LT + k^{-}_{T_m}\,DLT, \qquad (3.38)\\
&\quad + k^{-}_{T_m}\,TLT + k^{-}_{T_m}\,TLT' + k_{32}\,H_3ES,\\
\frac{dT_i}{dt} &= -\,(k^{+}_{T_i}\,L + k^{+}_{T_i}\,LT + k^{+}_{T_i}\,LD + k_p\,n_{vdac})\,T_i + k^{-}_{T_i}\,TL + k^{-}_{T_i}\,TLD, \qquad (3.39)\\
&\quad + k^{-}_{T_i}\,TLT + k^{-}_{T_i}\,TLT' + k_p\,T_{cyto}\,n_{vdac},\\
\frac{dT_{cyto}}{dt} &= n_{vdac}\,k_{vdac}\,T_c - n_{vdac}\,k_{vdac}\,T_{cyto}, \qquad (3.40)
\end{aligned}
$$

here $\mathrm{D_m}$ is the number of ADP molecules in the matrix, $\mathrm{T_m}$ is the number of ATP molecules in the matrix, $\mathrm{D_i}$ is the number of ADP molecules in the IMS, $\mathrm{T_i}$ is the number of ATP molecules in the IMS, $\mathrm{T_{cyto}}$ is the number of ATP molecules in the cytosol. These numbers were set by converting the concentration in each compartment to the number of molecules for each reconstruction (see subsection Metabolite buffers 3.4), these were the initial conditions considered. The number of VDACs on the OM is represented as $\mathrm{n_{vdac}}$ in these equations (this parameter is $\#\mathrm{VDACs_1}$ in Table 6 for reconstruction $\#1$).

As before, the rate constants of the bimolecular reactions have been normalized to have proper units to compute the number of particles, i.e. $\mathrm{k} = \frac{\mathrm{k'}}{\mathrm{N_A * V}}$, where $\mathrm{k'}$ represents the constants given in Table 4, $\mathrm{N_A}$ is the Avogadro's number, and V represents the volume.

As for the ATP synthase model, the total number of ANTs is a conserved quantity ($\mathrm{L_{tot}} = \mathrm{L} + \mathrm{DL} + \mathrm{DLD} + \mathrm{DLD'} + \mathrm{TL} + \mathrm{LT} + \mathrm{TLT} + \mathrm{TLT'} + \mathrm{DLT} + \mathrm{TLD}$). $\mathrm{L_{tot}}$ is the total number of ANTs considered in our simulations, for the mitochondrial reconstruction $\#1$ this quantity is 16471 (this parameter is $\#\mathrm{ANTs_1}$ in Table 4).

3.3. **Molecular VDAC Model.** The main mechanism for metabolites to cross the OM is through VDACs. To consider the ATP export from the IMS into the cytosol, we included VDACs. We implemented a rather simple model assuming VDAC proteins interact with ATP molecules and translocate them to the cytosol by the reaction $\mathrm{VDAC} + \mathrm{ATP_{IMS}} \rightleftharpoons \mathrm{VDAC} + \mathrm{ATP_{cyto}}$. The list of parameter values employed is given in Table 6.

Parameter	Definition	Value	Unit
$\mathrm{k_{vdac}}$	Rate constant of the reaction	1×10^6	$M^{-1}\ s^{-1}$
δ_{vdacs}	Density of VDACs on the OM	1×10^4	μm^{-2} (De Pinto et al., 1987)
$\#\ \mathrm{VDACs_1}$	Number of VDACs for Mito # 1	6340*	

TABLE 6. Parameters for the VDAC model. * We used the surface area of the OM to estimate the final number of VDACs from the density.

3.4. **Metabolite buffers.** The total concentration of ATP and ADP can be distributed in different compounds or states like ATP^{4-}, ADP^{3-}, $ATPMg^{2-}$, etc. ATP and ADP can react with different cations, be bound, or ionized. The final distributions can be estimated by coefficients representing the fraction of unbound ATP in the matrix or the other compartments, these proportions are determined mainly by the level of $\mathrm{Mg^{2+}}$. For our model, mitochondrial ADP^{3-} and ATP^{4-} concentrations were estimated analogously to previous work (Magnus and Keizer, 1997). These estimations are based on experimental data (Corkey et al., 1986). The approximate distributions are $[ADP]_{m,free}$ = 0.8 $[ADP]_m$, $[ATP]_{m,free}$=$[ATP]_m$, $[ATP^{4-}]$ = 0.05 $[ATP]_{free}$ and $[ADP^{-3}]$ = 0.45 $[ADP]_{free}$.

The initial concentrations of ATP and ADP in the IMS and cytosol were set to 6.5 mM and 0.1 mM (Mörikofer-Zwez and Walter, 1989; Cunningham et al., 1986). The initial concentrations of ATP and ADP in the matrix were set to 13 mM and 2 mM (15 mM in total). The total concentration of adenylates in the matrix (ATP + ADP) of liver mitochondria is in the range 2-27 mM (Rulfs

and Aprille, 1982; Nosek et al., 1990; Austin and Aprille, 1984), in the same range for heart mitochondria (Livingston et al., 1996) and also approximately 15 mM for pancreatic cells (Magnus and Keizer, 1997). Moreover, the ratio of ATP to ADP in the matrix has been estimated to be about 10 (Nicholls, 2013). These results are consistent with our assumption of an initial concentration of 13 mM of ATP and 2 mM of ADP in the matrix. In some simulations, these concentrations were kept constant. The concentrations were converted to number of molecules using the volumes of the different compartments (see Table 7).

3.5. **Simulation methods.**

System of ODEs. The system of ODEs has a total of 19 equations, and 41 parameters, including chemical rate constants, volumes, and number of proteins. The volumes of the different compartments are listed in Table 7, we used the reconstruction #1 for all the non-spatial simulations.

Equations 3.29, 3.37 and 3.40 were integrated using a Radau stiff integrator in PyDSTool (Clewley et al., 2007).

Spatial simulations. To perform spatiotemporal simulations in realistic 3D reconstructions we implemented the set of reactions in MCell version 4.0 (Kerr et al., 2008; Stiles et al., 1996; Husar et al., 2022), an agent-based reaction-diffusion simulator. The model is built giving the set of reactions described in Tables 1 and 3. Previous research showed that ATP synthases accumulate at the rim of the cristae membrane in lamellar cristae and along the length of tubular cristae (Strauss et al., 2008; Davies et al., 2012), to emulate this organization in our reconstructions we selected the areas of high curvature in the cristae membrane (Mendelsohn et al., 2021) and we randomly distributed them in these areas. The areas of high curvature were identified as vertices of the cristae membrane with first principal curvature higher than 70 μm^{-1}. The location of ANTs in mitochondria has not been definitively resolved, experimental evidence shows they may form complexes with ATP synthases (Ko et al., 2003) located in the CM (Wittig and Schägger, 2009; Vogel et al., 2006). Therefore, we randomly distributed ANTs in the areas of high curvature as well. VDACs were homogeneously distributed on the OM. ATP and ADP molecules were homogeneously distributed in the respective compartments. The diffusion coefficient considered for the free forms of ATP and ADP is 1.5×10^{-7} cm^2 s^{-1}.

3.5.1. *Supplementary Material.* In Figure 1 and Figure 2 in the supplementary material, we compared experimental results from (Kraemer and Klingenberg, 1982; Duyckaerts et al., 1980) to the results obtained with the ANT translocator model. In Figure 3 we show ATP fluxes through ANTs generated with the model developed by (Bohnensack, 1982). In Figure 4 we present spatial simulation performed with the same conditions considered in the main text, but keeping the number of ATP synthases constant in all reconstructions. In Figure 5, we compare the result with the previously developed version of the mitochondrial model (Garcia et al., 2019) with the current version.

Property	Mito 1	Mito 2	Mito 4	Mito 5	Mito 8	Mito 9	Mito 10	Mito 11	Mito 12
OM Vol (μm^3)	0.037	0.029	0.012	0.012	0.014	0.006	0.016	0.009	0.021
IM Vol (μm^3)	0.016	0.010	0.005	0.004	0.006	0.002	0.008	0.003	0.010
IM SA (μm^2)	1.545	1.104	0.505	0.390	0.508	0.224	0.605	0.314	0.806
high curva (μm^2)	0.087	0.049	0.037	0.015	0.042	0.032	0.067	0.023	0.115
Cyto Vol (μm^3)	0.306	0.061	0.094	0.048	0.101	0.050	0.108	0.111	0.148
# ATP_{syn}	267	150	114	46	129	98	204	72	353
# ANTs	16471	10 294	5398	4118	6177	2570	7905	3578	10294
# VDACs	6340	5990	2816	3370	3560	1788	3126	2558	3970

TABLE 7. Volumes and surface areas of the different compartments considered in the model. These measurements were taken from nine realistic 3D reconstructions of presynaptic and axonal mitochondria (Mendelsohn et al., 2021). The volume of the cytosol (Cyto Vol) is an arbitrary volume. The numbers of proteins considered for each simulation were determined using the densities (Tables 2,4, and 6) and the respective surface areas or volumes. To determined the number of ATP synthases the areas of high curvature (Mendelsohn et al., 2021) were considered (high curva IM SA), values of the first principal curvature larger than 70 μm^{-1} were assessed.

4. RESULTS

Before studying the dynamics of the assembled model, we first analyzed the behavior of its components separately and compared them with previously developed models. In these first simulations, we assumed steady-state conditions and kept the ADP and ATP concentrations constant in the different compartments. We then conducted dynamic simulations with the ODE representation to understand which is the limiting step in ATP production. Finally, we performed spatial simulations with nine realistic 3D geometries and related the ATP production rate to the morphology of the organelles.

4.1. **Steady-state flux analysis for the model components and comparison to previously developed models.** First, we analyzed the dependence of the ATP flux on the ADP concentration, membrane potential, and pH for the ATP synthase model. The driving forces of the cycle **c** (Figure 2C) are the membrane potential, the pH, and the ratio of the ADP and Pi concentration, to the ATP concentration relative to the equilibrium constant (Eq 3.26). For these simulations, the ΔpH was set to -0.4 (Tischler et al., 1977) and the total concentration of adenine nucleotides in the matrix was set to 15 mM (Austin and Aprille, 1984; Rulfs and Aprille, 1982). In Figure 3A, we show the ATP net flux through ATP synthases for different concentrations of ADP in the matrix. A positive flux is defined in the counter-clockwise direction, favoring ATP hydrolysis. We found that at small concentrations of ADP the flux is positive, meaning ATP is hydrolyzed. Increasing the concentration of ADP in the matrix, the ATP flux becomes negative, indicating that ATP synthesis is favored. The flux saturates for concentrations of ADP above 1 mM. Moreover, the driving forces of the cycle also depend on the membrane potential (Eq. 3.26). For a membrane potential

above 160 mV the ATP flux is negative, for large concentrations of ADP, but for membrane potential below those values ATP is hydrolyzed. Similar results were obtained for the ATP flux derived by Magnus and Keizer 1997, and later modified by Cortassa et al. 2003 (for comparison see Figure A6-A in the Supplementary Material by Cortassa et al. 2003, the difference in the sign of the fluxes is due to different sign conventions).
Next, we studied the dependence of the ATP flux on the pH difference between the matrix and the IMS (Figure 3B). Here, we fixed the pH in the matrix at 7.6 and varied the pH in the IMS. When the pH difference between the matrix and IMS is large, a smaller membrane potential is needed to observe a negative ATP flux, i.e. to synthesize ATP. This is because the proton motive force —the membrane potential minus the difference in pH (Eq. 3.21)— drives the protons to the matrix.

The ATP flux also saturates at higher membrane potentials, and in particular, it is almost saturated at 180 mV —the potential considered for the rest of this work. Similar flux dependencies were observed in the past (for comparison see Figure A6-B in the Supplementary Material by Cortassa et al. 2003). Although their maximal flux is about 10 mM s^{-1} while ours is about 0.9 mM s^{-1}. A similar dependence on the membrane potential was also observed by Nguyen et al. 2007 (Figure 2D in their paper), their maximum flux is 1.125 mM s^{-1} very close to the range in our work.

The driving force of the ANT translocation is the membrane potential and the ratio of $\mathrm{ATP_m/ADP_m}$ in the matrix and $\mathrm{ATP_i/ADP_i}$ in the IMS (Eq. 3.33). Therefore, we studied the dependence of the net $\mathrm{ADP_i} - \mathrm{ATP_m}$ flux through ANTs at steady concentrations of ATP and ADP, for different ratios. First, we calculated the net $\mathrm{ADP_i} - \mathrm{ATP_m}$ flux through ANTs for different ratios $\mathrm{ATP_m/ADP_m}$ in the matrix (Figure 4A). Keeping the cytosolic ratio fixed at 65, we varied the $\mathrm{ATP_m/ADP_m}$ ratio. The driving force of the cycle (Eq. 3.33) increases for larger $\mathrm{ATP_m/ADP_m}$ ratios, increasing the net $\mathrm{ADP_i} - \mathrm{ATP_m}$ flux (Figure 4A). The net $\mathrm{ADP_i} - \mathrm{ATP_m}$ flux saturates for ratios $\mathrm{ATP_m/ADP_m}$ closer to the ratio of $\mathrm{ATP_i/ADP_i}$ (Eq. 3.33).

Next, we varied the $\mathrm{ATP_i/ADP_i}$ ratio in the IMS and kept the matrix ratio constant at 6.5. Increasing the $\mathrm{ATP_i/ADP_i}$ ratio decreases the driving force (Eqs. 3.33) at constant $\mathrm{ATP_m/ADP_m}$ ratio. Therefore, the net $\mathrm{ADP_i} - \mathrm{ATP_m}$ flux decreases for larger ratios of $\mathrm{ATP_i/ADP_i}$ (Figure 4B). Moreover, the maximum flux is set by the $\mathrm{ATP_m/ADP_m}$ ratio. Similar flux dependencies were found by Magnus and Keizer 1997 with the model developed by Bohnensack 1982, see the Supplementary Figure 3.

From this analysis, we identified that for 1 mM $\mathrm{ADP_m}$, 180 mV membrane potential, and -0.4 ΔpH, the ATP flux is almost at its maximum absolute value (Figure 3A-B). We used these values for the rest of this work. Likewise, the initial concentration ratios considered in the rest of this work are $\mathrm{ATP_m/ADP_m} = 6.5$ and $\mathrm{ATP_i/ADP_i} = 65$, from which the $\mathrm{ADP_i} - \mathrm{ATP_m}$ flux through ANTs is almost at its maximal value.

4.2. **Under physiological conditions, ATP production is the limiting step for cytosolic ATP availability.** The amount of ATP in the cytosol depends on the production rate and its export through ANTs and VDACs. Since experimental results suggest that the ANT translocation rate

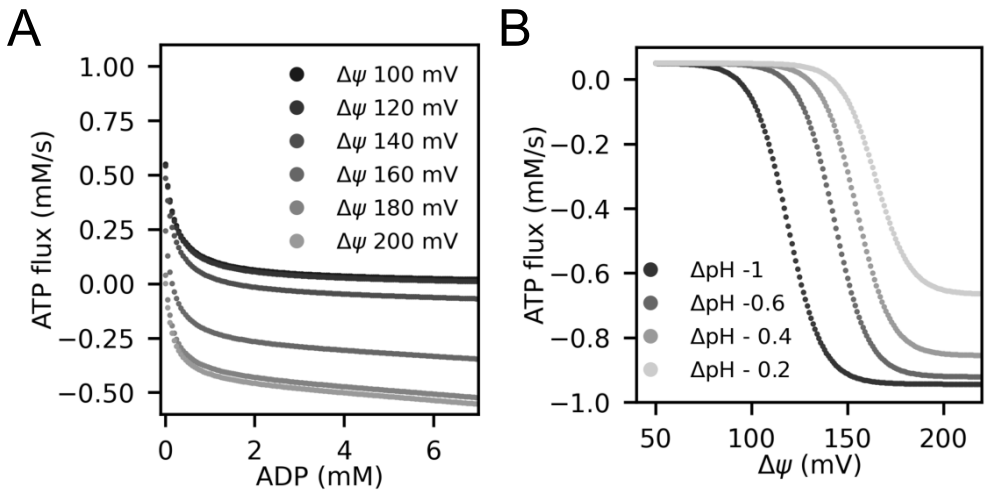

FIGURE 3. ATP synthase steady-state flux analysis. We analyzed the dependence on the fluxes through ATP synthases at constant concentrations of adenine nucleotides in the different compartments. We analyzed how the flux changes with the driving forces of the cycles (Eqs. 3.26). A) ATP net flux through ATP synthases for different concentrations of ADP in the matrix and different membrane potentials. A counter-clockwise cycle is defined as positive, favoring ATP hydrolysis. For membrane potential above 160 mV and larger $\mathrm{ADP_m}$ concentrations, ATP is synthesized. B) ATP net flux through ATP synthases for different pH and membrane potentials (for fixed concentrations of adenine nucleotides).

constants are in the order of 100s per second (Gropp et al., 1999), we explored the impact of fast export through ANTs on the final ATP concentration in the cytosol. We held the concentration of ADP in the IMS constant and changed the parameters of the ANT model. Specifically, we changed the value of the rate constants $\mathrm{k_p}$, $\mathrm{k_{cp}}$, $\mathrm{k_t}$, and $\mathrm{k_d}$ multiplying them by a factor r, such that detailed balance is still satisfied. We measured the number of ADP and ATP molecules in the matrix (Figure 5A-B), and the number of molecules of ATP in the IMS and cytosol (Figure 5C-D). Faster translocation allows more ADP to accumulate in the matrix (Figure 5A) and therefore less ATP (Figure 5B), while ATP molecules reach the IMS and the cytosol faster (Figure 5C-D). We further calculated the percentage of the ATP increase relative to the slowest import (Figure 5E). The fastest ANTs (r = 10) exports 5% more ATP molecules than the slowest ones. Moreover, the amount of ATP starts to saturate for the fastest ANTs (r = 10). This means even ANTs that are faster cannot overcome the ATP production rate. Thus, the rate-limiting step is the ATP production rate, not the export.

In addition to the translocation rate of the ANTs, the ratio of ANTs to the ATP synthases can influence the export of ATP molecules into the cytosol. Therefore, we next asked how this ratio affects the availability of ATP in the cytosol for the fastest ANTs. We asked which step limits the number of ATP molecules in the cytosol under these conditions – is it the synthesis of ATP or its translocation through ANTs? As in the previous simulations, the number of ADP molecules in

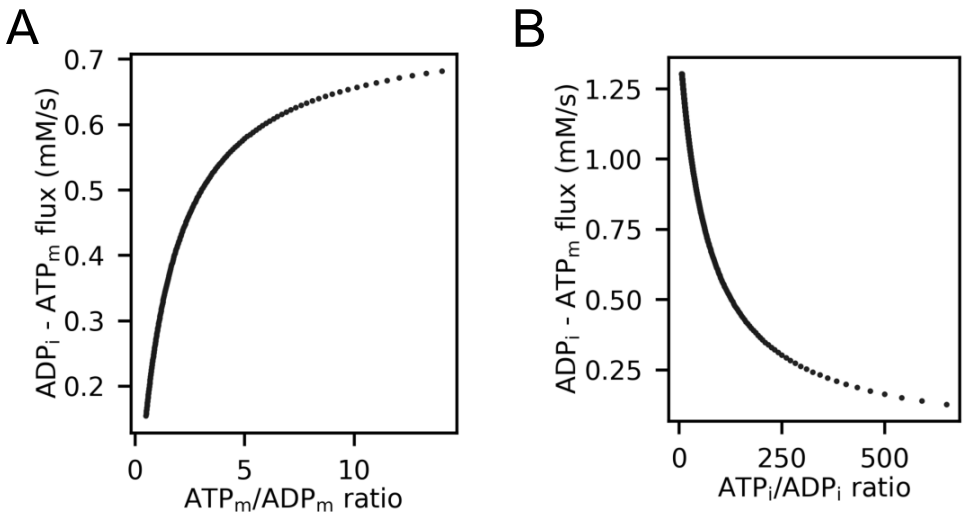

FIGURE 4. ANT steady-state flux analysis. We analyzed the dependence on the fluxes through ANTs at constant concentrations of adenine nucleotides in the different compartments and at a constant membrane potential of 180 mV. We analyzed how the flux changes with the driving forces of the cycles (Eqs. 3.33). A) $\mathrm{ADP_i} - \mathrm{ATP_m}$ net flux through ANTs for different ATP to ADP ratios in the matrix. B) $\mathrm{ADP_i} - \mathrm{ATP_m}$ net flux through ANTs for different ratios of ATP and ADP in the IMS.

the IMS was constant, assuming unlimited resources. We measured the number of ADP and ATP molecules in the matrix, IMS, and cytosol over time (Figure 6A-D).

The amount of ATP in the cytosol after 1 second starts to saturate when the number of ANTs is twenty times the number of ATP synthases (Figure 6E). Thus our model predicts that having more than twenty times ANTs to ATP synthases number will not have any benefit. If this ratio is bigger than twenty, the limiting step is the production of ATP.

Similarly, VDACs can limit the amount of ATP in the cytosol. Therefore, we analyzed how the export of ATP through VDACs limits their amount in the cytosol. Considering similar conditions as before constant concentration of ADP in the IMS, we changed the number of VDACs in the OM and measured the number of ADP and ATP in the different compartments (Figure 7A-D), along with the percentage increment of ATP in the cytosol after 1 second (Figure 7F). Having less than approximately 500 VDACs in the OM significantly limits the amount of ATP available in the cytosol. Otherwise, the production of ATP is the limiting step.

Given the density of VDACs in the OM (De Pinto et al., 1987) and the surface area of the OM measured (Mendelsohn et al., 2021) (see Methods), the number of VDACs in the reconstruction #1 is 6340. This number is well above the limiting threshold of 500. Therefore, in the physiological conditions we considered, the production of ATP is the limiting step.

4.3. **Spatial Simulations: application of the model to different 3D mitochondrial reconstructions.** To illustrate the utility of our model, we conducted spatial simulations with nine realistic

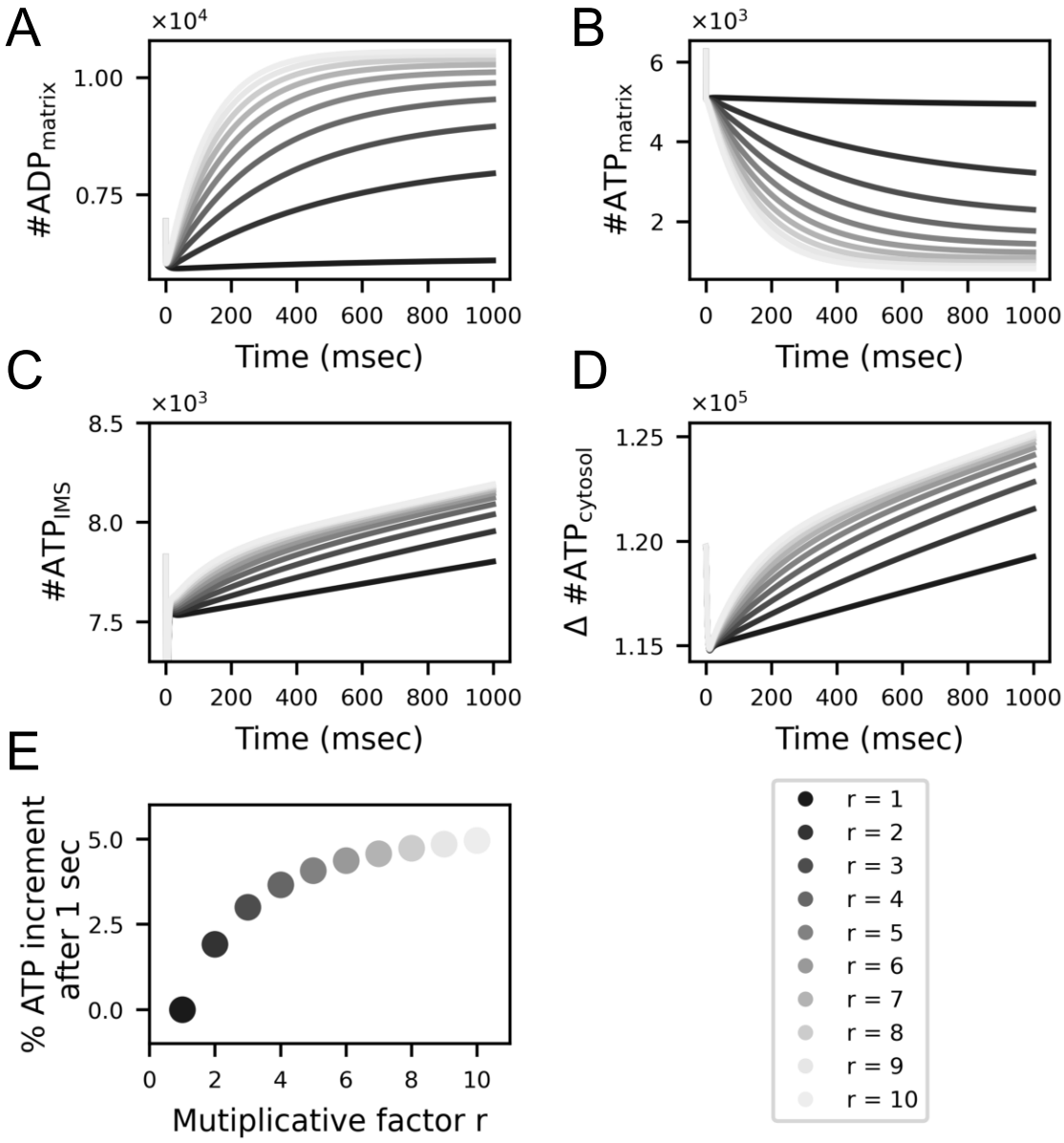

FIGURE 5. Parameter exploration for the ANT model at a constant membrane potential of 180 mV. We employed the ODE model to explore the impact of faster ANTs on ATP production, for that, we changed the rate constants of the ANTs. We multiplied the rate constants k_p, k_{cp}, k_t, and k_d by a factor r, where r takes values between 1 and 10. The ADP concentration in the IMS was kept constant in these simulations. (A)-(C) Number of molecules measured over time in the different compartments. (D) Number of ATP molecules measured over time in the cytosol relative to the initial number of molecules. (E) Percentage increment of the number of ATP molecules in the cytosol after 1 second relative to the slowest ones (r = 1), for all ANTs considered from the slowest (r = 1) ones to the fastest ones (r = 10).

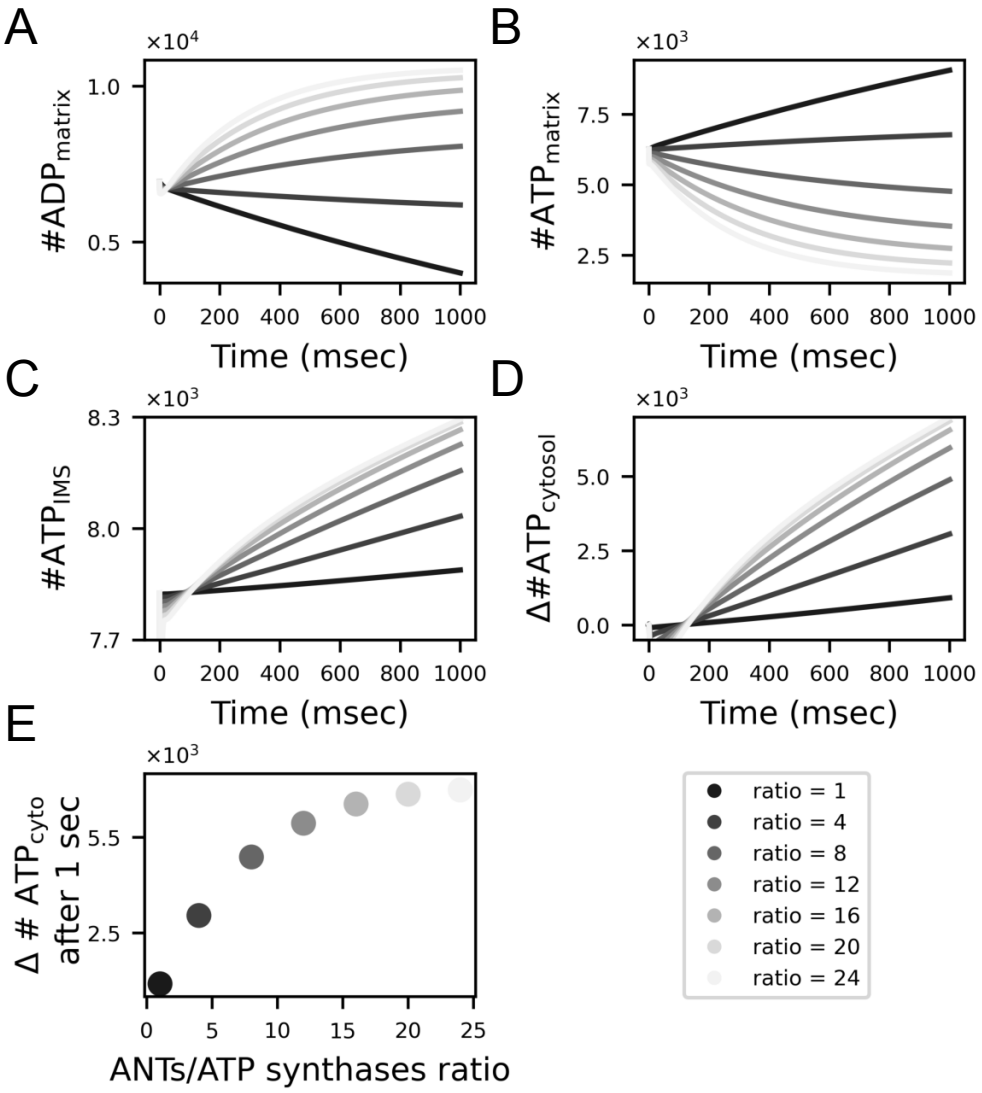

FIGURE 6. What is the limiting factor, export through ANTs or production of ATP through ATP synthases? We changed the ratio of ANTs to ATP synthases to answer this question and used the ODE model to estimate the impact on ATP production, for a constant concentration of ADP in the IMS and a constant membrane potential of 180 mV. (A)-(C) Number of molecules measured over time in the different compartments. (D) Number of ATP molecules measured over time in the cytosol relative to the initial number. (E) Number of ATP molecules in the cytosol after 1 second relative to the initial number of molecules, for different ratios of ANTs/ATP synthases. Ratios go from 1 to 24, the number of ATP synthases is kept constant and the number of ANTs increases (fast ANTs were considered r = 10).

3D reconstructions (Mendelsohn et al., 2021), using the agent-based reaction-diffusion simulator MCell, and we related the ATP production rate to morphological features of mitochondria. In Figure 8A we show the CM of the nine reconstructions with the total number of ATP synthases

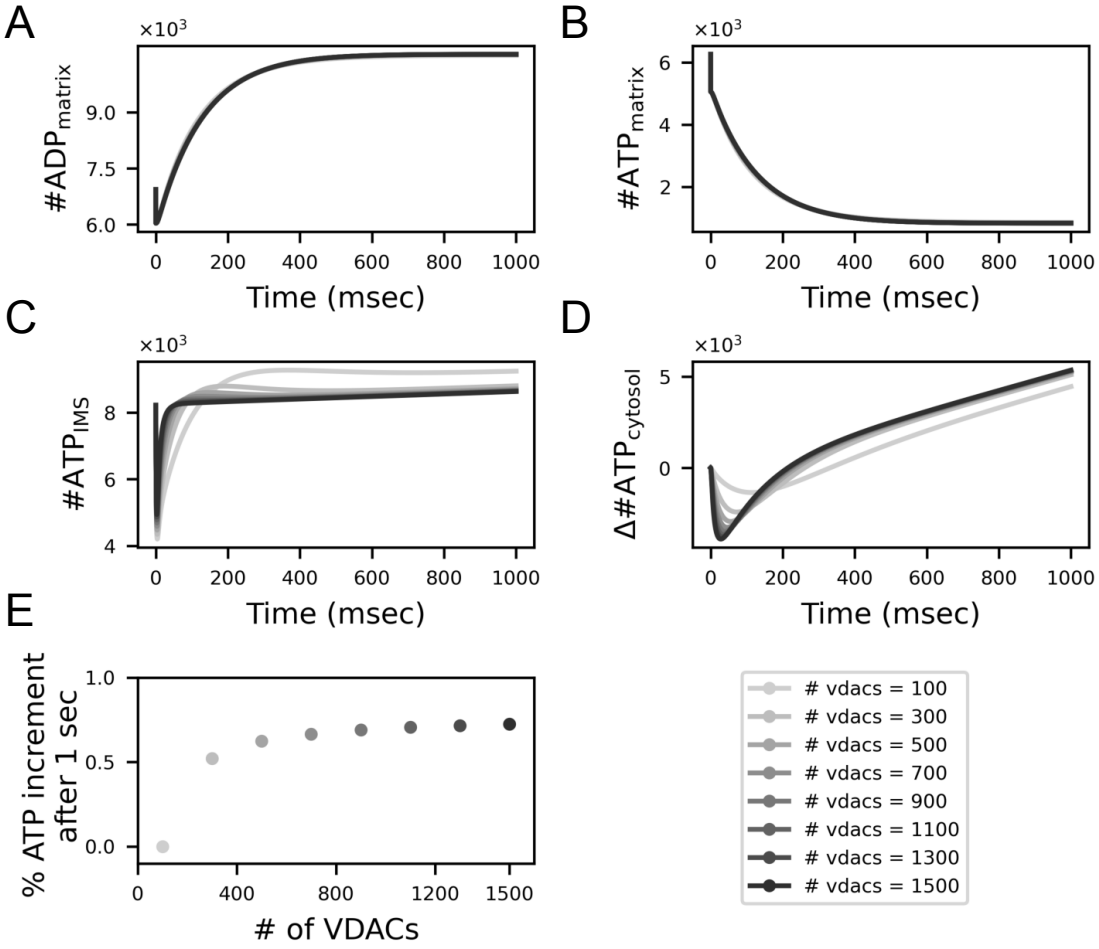

FIGURE 7. Effect of the number of VDACs on ATP efflux to the cytosol at a constant membrane potential of 180 mV. (A)-(C) Number of molecules measured over time in the different compartments. (D) Number of ATP molecules measured over time in the cytosol relative to the initial concentration. (E) Percentage increase of ATP in the cytosol after 1 second for different numbers of VDACs in the OM. The number of VDACs goes from 100 to 1500 (in these simulations fast ANTs were considered, r = 10).

considered for the simulations (in red). In Figure 8B we show the results of the ODE system and averaged traces of the spatial simulations (over ten different realizations) of the number of ADP and ATP in the different compartments for the elongated mitochondrial reconstruction #2, for the same conditions considered as before.

Using tools from differential geometry, we recently analyzed structural features of these reconstructions and based on this analysis we group them in two categories: globular organelles and elongated ones (Mendelsohn et al., 2021) (Figure 8A). Organelles in the globular group have larger surface area formed by vertices with high curvature. Large curved surface areas correspond to more number of ATP synthases in these reconstructions.

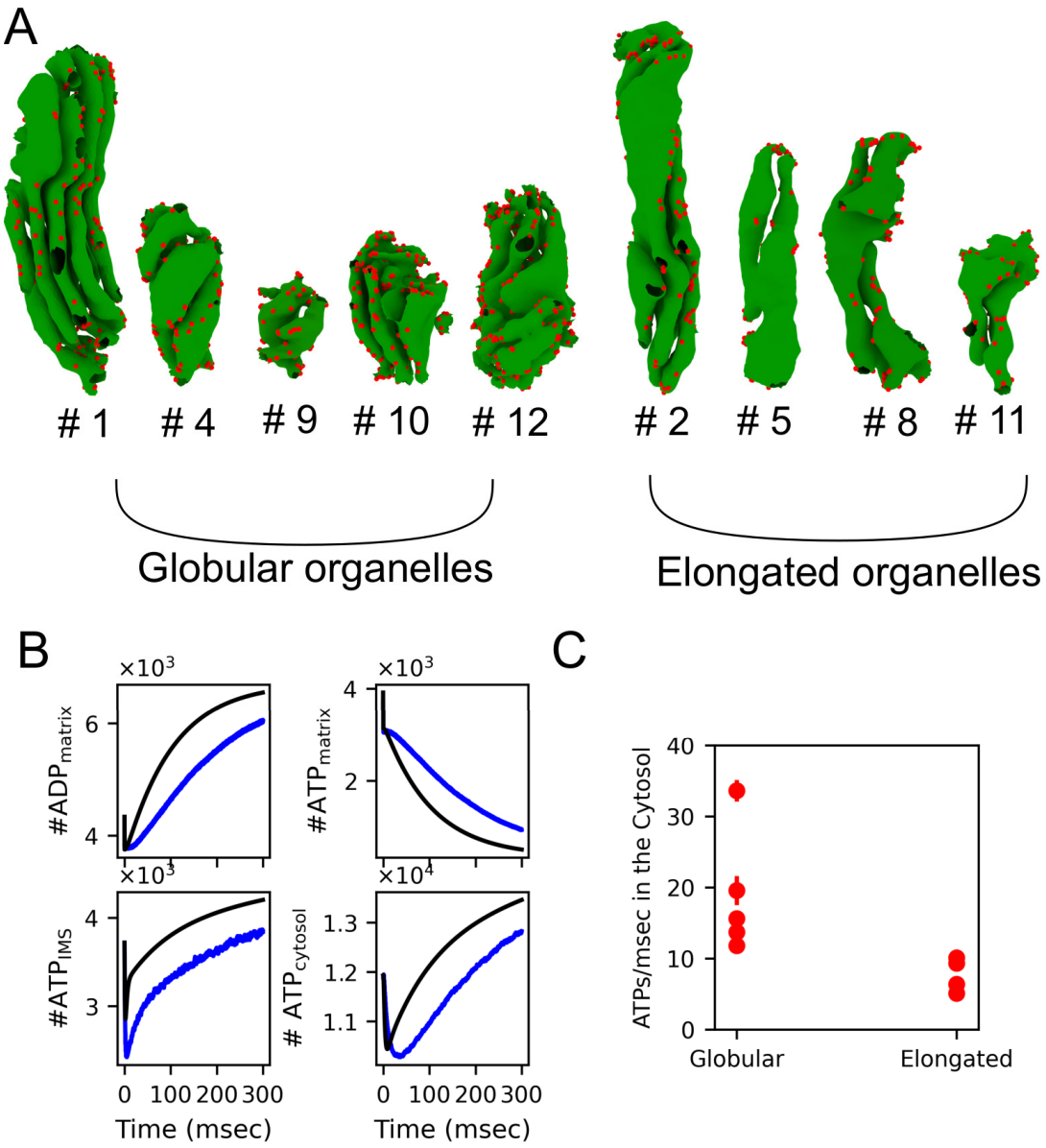

FIGURE 8. Spatial simulations: linking structure to function. A) Cristae membrane of the nine mitochondrial reconstructions considered with ATP synthases (in red) distributed in the areas of high curvature. B) Comparison of the ODEs simulations with the average traces of the spatial simulations for elongated mitochondrial reconstruction #2. C) ATP production rate in the cytosol for all reconstructions grouped accordingly to the structural features.

We performed spatial simulations for all reconstructions and we measured the ATP production rate in the cytosol for each reconstruction. For that, we performed a linear regression to single traces of the number of ATP molecules in the cytosol over time. Averaged rates are shown in Figure 8C. As expected from our analysis the ATP production rate in the cytosol is larger for globular organelles, which have larger areas of high curvature.

5. Discussion

Given the indispensable nature of mitochondria in cellular energy production, having accurate models of mitochondrial dynamics is critical for understanding their impact on cellular function.

In this work, we focused on developing a thermodynamically consistent model of ATP production in mitochondria to ensure the model is physically plausible. In doing so, we derived the relationships for the dependence of kinetic parameters on the membrane potential, proton and substrate concentration.
We explored different parameter regimes to understand in which conditions ATP production or its export are the limiting steps in making ATP available in the cytosol. Under the conditions considered, we found two regimes: at a low ratio of ANTs to ATP synthases, the export of ATP is limited by the ANTs. At ratios higher then 20:1, the ATP production becomes the limiting step. Similarly, the number of VDACs does not limit the export of ATP, unless there are very few VDACs present (in the order of 100s, for the ratio of ANTs/ATP synthases considered).

Finally, we performed spatial simulations on nine mitochondrial reconstructions derived from electron microscopy data. According to our parameter exploration, the number of ANTs and VDACs in these nine reconstructions are such that the synthesis of ATP is the limiting step on the ATP production rate in the cytosol and not its export. We further measured the rate for the same conditions, and relate this quantity to structural features of the organelles. We had mapped features of the OM to features of the IM recently in Mendelsohn et al. 2021 with tools from differential geometry and showed that globular organelles —characterized by smaller aspect ratio and smaller average first principal curvature of the OM— have larger curved CM surface areas. These organelles also have other features of high energy capacity like large crista shape factor and a high number of crista junctions per OM surface area. Others have shown that mitochondria at high-energy demanding locations in outer hair cells of young mice (Perkins et al., 2020) as well as mitochondria from high-spiking interneurons (Cserép et al., 2018) show a large crista shape factor and a high number of crista junctions per OM surface area. These features are also characteristic of our globular set, which suggests a high level of metabolic activity for such mitochondria. Here, using our mathematical model we found globular organelles generate more ATP in the cytosol than the elongated morphologies (Figure 8C).
The maximum rate measured with our spatial model is roughly 30 ATPs/ms (Figure 8C), this corresponds to $170\,\mu\mathrm{M\,s^{-1}}$ (considering the volume of the cytosol). Recent measurements in myocytes (Wescott et al., 2019) estimated the ATP production rate in the range 200-600 $\mu\mathrm{M\,s^{-1}}$ depending on the calcium concentration. The organelles considered in this manuscript are axonal and presynaptic reconstructions and are small (in the range of 0.037 to $0.012\,\mu\mathrm{m}^3$) compared to organelles in myocytes (in the order of $0.5\,\mu\mathrm{m}^3$ (Laguens, 1971)). This could explain our smaller ATP production rate in the cytosol.

We acknowledge that our modeling approach has a number of limitations. First, the membrane potential in our simulations is constant, we emulate a constant state of ATP production. Second,

the ATP synthase flux considered in our model saturates sigmoidally at a large membrane potential (Figure 3B), as it has been shown for P. modestum bacteria and E. coli (Kaim and Dimroth, 1999), and is more sensitive to changes in the membrane potential than to ΔpH. However, recent experiments on heart and skeletal mitochondria (Wescott et al., 2019) show no saturation of the ATP synthase flux when increasing the membrane potential. Our model does not reproduce this behavior. Its voltage-dependence is a consequence of the detailed dynamic of ATP synthase model (Pietrobon and Caplan, 1985), which is drawn from physical assumptions about the rate constants, the membrane potential, and the pH concentration. Taking different assumptions or expanding the number of states could perhaps give a different flux membrane potential dependence. Third, the Mg^{2+}-bound forms of ADP and ATP are the main substrate of ATP synthase in mitochondria. Since our goal was to generate a spatial model of a mitochondrion and Mg^{2+} is in large concentration in the matrix, we considered the free form of ADP as the main substrate for ATP production. This is an approximation, due to the limitations of using an agent-based model. However, this approximation has been taken in many mitochondrial models in the past (Magnus and Keizer, 1997; Bertram et al., 2006; Cortassa et al., 2003) and it is accepted in the community (Gnaiger, 2020).

Different approaches can be taken to model the spatial organization of mitochondria. From continuum approximations (Leung et al., 2021; Afzal et al., 2021) to discrete descriptions as we considered in our spatial simulations (with an agent-based reaction-diffusion simulator). Well-mixed continuum approximations based on concentrations like those in (Leung et al., 2021; Afzal et al., 2021) break down at low particle numbers. A discrete particle-based approach, as we considered in our spatial simulations with an agent-based reaction-diffusion simulator, is more accurate in this scenario (Bartol et al., 2015). Continuum approaches could be more challenging to integrate in complex geometries. Since we want to explore the impact of the complex mitochondrial morphology on ATP production and include the specialized location of ATP synthases at the rim of the cristae we opted for a discrete description in our spatial simulations.

These different approaches can lead to similar results. For instance, in the past we observed gradients of ATP with our discrete approach (Garcia et al., 2019) and so did (Afzal et al., 2021) with a continuum description. Our earlier version of the model (Garcia et al., 2019) is based on the same published data (Pietrobon and Caplan, 1985; Metelkin et al., 2006; Magnus and Keizer, 1997). The major improvement of the current version is that the parameters were constrained by thermodynamic considerations (Hill, 1989). The results, however, are consistent (in Supplementary Figure 5 we compare for reconstruction # 1 both versions of the model).

Finally, our results have implications for our understanding of disease states. For instance, near total loss of ATP synthase dimerization caused by a neurodegenerative mutation generated profound disturbances of mitochondrial crista ultrastructure in neurons derived from a Leigh syndrome patient (Siegmund et al., 2018). The main architectural feature different than in control cells is an increment in the angle of curvature at the tips of the cristae. This feature relates to our curvature measurement of the CM, which directly relates to the total number of ATP synthases. Altered mitochondrial structures have also been shown in aged animals (Perkins et al., 2020; Glavis-Bloom

et al., 2023). Further investigation using the methods developed here will allow a deeper understanding of potentially impaired mitochondrial mechanisms in disease states.

6. Data Availability

All the material associated with this work is available in the repository:

`https://github.com/RangamaniLabUCSD/spatial_mito_model`

7. Acknowledgments

This work was supported by Air Force Office of Scientific Research (AFOSR) Multidisciplinary University Research Initiative (MURI) grant FA9550-18-1-0051 (to P. Rangamani) and Office of Naval Research N00014-20-1-2469 (to P. Rangamani). All authors declare no known or potential conflict of interest including any financial, personal, or other relationships with other people or organizations that could inappropriately influence, or be perceived to influence their work.

References

Acehan, D., Malhotra, A., Xu, Y., Ren, M., Stokes, D. L., and Schlame, M. 2011. Cardiolipin affects the supramolecular organization of atp synthase in mitochondria. *Biophysical journal*, 100(9):2184–2192.

Afzal, N., Lederer, W. J., Jafri, M. S., and Mannella, C. A. 2021. Effect of crista morphology on mitochondrial atp output: A computational study. *Current research in physiology*, 4:163–176.

Alberts, B., Roberts, K., Lewis, J., Bray, D., Hopkin, K., Johnson, A. D., Walter, P., and Raff, M. 2015. *Essential cell biology*. Garland Science.

Austin, J. and Aprille, J. 1984. Carboxyatractyloside-insensitive influx and efflux of adenine nucleotides in rat liver mitochondria. *Journal of Biological Chemistry*, 259(1):154–160.

Balbir, T. 2007. A model of mitochondrial calcium induced calcium release. *Doctoral dissertation The Ohio State University*.

Bartol, T. M., Keller, D. X., Kinney, J. P., Bajaj, C. L., Harris, K. M., Sejnowski, T. J., and Kennedy, M. B. 2015. Computational reconstitution of spine calcium transients from individual proteins. *Frontiers in synaptic neuroscience*, 7:17.

Beard, D. A. 2005. A biophysical model of the mitochondrial respiratory system and oxidative phosphorylation. *PLoS computational biology*, 1(4):e36.

Bertram, R., Gram Pedersen, M., Luciani, D. S., and Sherman, A. 2006. A simplified model for mitochondrial atp production. *Journal of Theoretical Biology*, 243(4):575–586.

Bohnensack, R. 1982. The role of the adenine nucleotide translocator in oxidative phosphorylation. a theoretical investigation on the basis of a comprehensive rate law of the translocator. *Journal of Bioenergetics and Biomembranes*, 14:45–61.

Caplan, S. 1981. Reciprocity or near-reciprocity of highly coupled enzymatic processes at the multidimensional inflection point. *Proc. Natl Acad. Sci. USA*, 78(7):4314–4318.

Caplan, S. R. and Essig, A. 1983. *Bioenergetics and linear nonequilibrium thermodynamics*. Harvard University Press.

Clewley, R. H., Sherwood, W. E., LaMar, M. D., and Guckenheimer, J. M. 2007. PyDSTool, a software environment for dynamical systems modeling.

Colombini, M. 2004. Vdac: the channel at the interface between mitochondria and the cytosol. *Molecular and cellular biochemistry*, 256(1):107–115.

Corkey, B. E., Duszynski, J., Rich, T. L., Matschinsky, B., and Williamson, J. R. 1986. Regulation of free and bound magnesium in rat hepatocytes and isolated mitochondria. *Journal of Biological Chemistry*, 261(6):2567–2574.

Cortassa, S., Aon, M. A., Marban, E., Winslow, R. L., and O'Rourke, B. 2003. An integrated model of cardiac mitochondrial energy metabolism and calcium dynamics. *Biophysical Journal*, 84:2734–2755.

Cserép, C., Pósfai, B., Schwarcz, A. D., and Dénes, Á. 2018. Mitochondrial ultrastructure is coupled to synaptic performance at axonal release sites. *Eneuro*, 5(1).

Cunningham, C. C., Malloy, C. R., and Radda, G. K. 1986. Effect of fasting and acute ethanol administration on the energy state of in vivo liver as measured by 31p-nmr spectroscopy. *Biochimica et Biophysica Acta (BBA)-Molecular Cell Research*, 885(1):12–22.

Davies, K. M., Anselmi, C., Wittig, I., Faraldo-Gómez, J. D., and Kühlbrandt, W. 2012. Structure of the yeast f1fo-atp synthase dimer and its role in shaping the mitochondrial cristae. *Proceedings of the National Academy of Sciences*, 109(34):13602–13607.

De Pinto, V., Ludwig, O., Krause, J., Benz, R., and Palmieri, F. 1987. Porin pores of mitochondrial outer membranes from high and low eukaryotic cells: biochemical and biophysical characterization. *Biochimica et Biophysica Acta (BBA) - Bioenergetics*, 894(2):109–119.

Duyckaerts, C., Sluse-Goffart, C. M., Fux, J. P., Sluse, F. E., and Lièbecq, C. 1980. Kinetic mechanism of the exchanges catalysed by the adenine-nucleotide carrier. *European Journal of Biochemistry*, 106(1):1–6.

Garcia, G. C., Bartol, T. M., Phan, S., Bushong, E. A., Perkins, G., Sejnowski, T. J., Ellisman, M. H., and Skupin, A. 2019. Mitochondrial morphology provides a mechanism for energy buffering at synapses. *Scientific reports*, 9.

Glavis-Bloom, C., Vanderlip, C. R., Weiser Novak, S., Kuwajima, M., Kirk, L., Harris, K. M., Manor, U., and Reynolds, J. H. 2023. Violation of the ultrastructural size principle in the dorsolateral prefrontal cortex underlies working memory impairment in the aged common marmoset (callithrix jacchus). *Frontiers in Aging Neuroscience*, 15:1146245.

Gnaiger, E. e. a. 2020. Mitochondrial physiology. *Bioenergetics Communications*.

Gropp, T., Brustovetsky, N., Klingenberg, M., Müller, V., Fendler, K., and Bamberg, E. 1999. Kinetics of electrogenic transport by the ADP/ATP carrier. *Biophysical Journal*, 77(2):714–726.

Heiske, M., Letellier, T., and Klipp, E. 2017. Comprehensive mathematical model of oxidative phosphorylation valid for physiological and pathological conditions. *The FEBS Journal*, 284(17):2802–2828.

Hill, T. L. 1989. *Free Energy Transduction and Biochemical Cycle Kinetics*. Academic Press.

Holmuhamedov, E. L., Jovanovic, S., Dzeja, P. P., Jovanovic, A., and Terzic, A. 1998. Mitochondrial atp-sensitive k+ channels modulate cardiac mitochondrial function. *American Journal of Physiology-Heart and Circulatory Physiology*, 275(5):H1567–H1576.

Husar, A., Ordyan, M., Garcia, G. C., Yancey, J. G., Saglam, A. S., Faeder, J., Bartol Jr, T. M., and Sejnowski, T. J. 2022. Mcell4 with bionetgen: A monte carlo simulator of rule-based reaction-diffusion systems with python interface. *bioRxiv*, pages 2022–05.

Kaim, G. and Dimroth, P. 1999. Atp synthesis by f-type atp synthase is obligatorily dependent on the transmembrane voltage. *The EMBO Journal*, 18(15):4118–4127.

Keener, J. P. and Sneyd, J. 1998. *Mathematical physiology*, volume 1. Springer.

Kerr, R. A., Bartol, T. M., Kaminsky, B., Dittrich, M., Chang, J.-C. J., Baden, S. B., Sejnowski, T. J., and Stiles, J. R. 2008. Fast monte carlo simulation methods for biological reaction-diffusion systems in solution and on surfaces. *SIAM journal on scientific computing*, 30(6):3126–3149.

Ko, Y. H., Delannoy, M., Hullihen, J., Chiu, W., and Pedersen, P. L. 2003. Mitochondrial ATP synthasome cristae-enriched membranes and a multiwell detergent screening assay yield dispersed single complexes containing the ATP synthase and carriers for Pi and ADP/ATP. *Journal of Biological Chemistry*, 278(14):12305–12309.

Kraemer, R. and Klingenberg, M. 1982. Electrophoretic control of reconstituted adenine nucleotide translocation. *Biochemistry*, 21(5):1082–1089.

Laguens, R. 1971. Morphometric study of myocardial mitochondria in the rat. *The Journal of cell biology*, 48(3):673.

Leung, A., Ohadi, D., Pekkurnaz, G., and Rangamani, P. 2021. Systems modeling predicts that mitochondria er contact sites regulate the postsynaptic energy landscape. *NPJ systems biology and applications*, 7(1):26.

Livingston, B. E., Altschuld, R. A., and Hohl, C. M. 1996. Metabolic compartmentalization in neonatal swine myocytes. *Pediatric research*, 40(1):59–65.

Magnus, G. 1995. *A mitochondria-based model for bursting and its D-glucose dependence in the pancreatic beta cell*. University of California, Davis.

Magnus, G. and Keizer, J. 1997. Minimal model of beta-cell mitochondrial Ca^{2+} handling. *American Journal of Physiology-Cell*, 273:C717 – C733.

Mendelsohn, R., Garcia, G. C., Bartol, T. M., Lee, C. T., Khandelwal, P., Liu, E., Spencer, D. J., Husar, A., Bushong, E. A., Phan, S., Perkins, G., Ellisman, M. H., Skupin, A., Sejnowski, T. J., and Rangamani, P. 2021. Morphological principles of neuronal mitochondria. *Journal of Comparative Neurology*.

Metelkin, E., Goryanin, I., and Demin, O. 2006. Mathematical modeling of mitochondrial adenine nucleotide translocase. *Biophysical Journal*, 90(2):423–432.

Mörikofer-Zwez, S. and Walter, P. 1989. Binding of adp to rat liver cytosolic proteins and its influence on the ratio of free atp/free adp. *Biochemical Journal*, 259(1):117–124.

Nguyen, M.-H. T., Dudycha, S. J., and Jafri, M. S. 2007. Effect of ca2+ on cardiac mitochondrial energy production is modulated by na+ and h+ dynamics. *American Journal of Physiology-Cell Physiology*, 292(6):C2004–C2020.

Nicholls, D. G. 2013. *Bioenergetics*. Elsevier Science.

Nosek, M. T., Dransfield, D., and Aprille, J. 1990. Calcium stimulates atp-mg/pi carrier activity in rat liver mitochondria. *Journal of Biological Chemistry*, 265(15):8444–8450.

Pekkurnaz, G. and Wang, X. 2022. Mitochondrial heterogeneity and homeostasis through the lens of a neuron. *Nature Metabolism*, 4(7):802–812.

Perkins, G., Lee, J. H., Park, S., Kang, M., Perez-Flores, M. C., Ju, S., Phillips, G., Lysakowski, A., Gratton, M. A., and Yamoah, E. N. 2020. Altered outer hair cell mitochondrial and subsurface cisternae connectomics are candidate mechanisms for hearing loss in mice. *Journal of Neuroscience*, 40(44):8556–8572.

Pietrobon, D. and Caplan, S. R. 1985. Flow-force relationships for a six-state proton pump model: Intrinsic uncoupling, kinetic equivalence of input and output forces, and domain of approximate linearity. *Biochemistry*, 24(21):5764–5776.

Rulfs, J. and Aprille, J. R. 1982. Adenine nucleotide pool size, adenine nucleotide translocase activity, and respiratory activity in newborn rabbit liver mitochondria. *Biochimica et Biophysica Acta (BBA)-Bioenergetics*, 681(2):300–304.

Siegmund, S. E., Grassucci, R., Carter, S. D., Barca, E., Farino, Z. J., Juanola-Falgarona, M., Zhang, P., Tanji, K., Hirano, M., Schon, E. A., et al. 2018. Three-dimensional analysis of mitochondrial crista ultrastructure in a patient with leigh syndrome by in situ cryoelectron tomography. *iScience*, 6:83–91.

Stiles, J. R., Van Helden, D., Bartol, T., Salpeter, E. E., and Salpeter, M. M. 1996. Miniature endplate current rise times less than 100microseconds from improved dual recordings can be modeled with passive acetylcholine diffusion from a synaptic vesicle. *Proceedings of the National Academy of Sciences*, 93(12):5747–5752.

Strauss, M., Hofhaus, G., Schröder, R. R., and Kühlbrandt, W. 2008. Dimer ribbons of atp synthase shape the inner mitochondrial membrane. *The EMBO journal*, 27(7):1154–1160.

Tischler, M. E., Hecht, P., and Williamson, J. R. 1977. Determination of mitochondrial/cytosolic metabolite gradients in isolated rat liver cells by cell disruption. *Archives of biochemistry and biophysics*, 181(1):278–292.

Vogel, F., Bornhövd, C., Neupert, W., and Reichert, A. S. 2006. Dynamic subcompartmentalization of the mitochondrial inner membrane. *J. Cell Biol.*, 175(2):237–247.

Wescott, A. P., Kao, J. P., Lederer, W. J., and Boyman, L. 2019. Voltage-energized calcium-sensitive atp production by mitochondria. *Nature Metabolism*, 1(10):975–984.

Wittig, I. and Schägger, H. 2009. Supramolecular organization of ATP synthase and respiratory chain in mitochondrial membranes. *Biochimica et Biophysica Acta (BBA)-Bioenergetics*, 1787(6):672–680.

Yoshida, M., Muneyuki, E., and Hisabori, T. 2001. Atp synthase-a marvellous rotary engine of the cell. *Nature reviews Molecular cell biology*, 2(9):669.